Syn-Eruptive Processes as Recorded By Crystals and Vesicles in The Bishop Tuff, California: A Combination Of Experimental Petrology and 3D Imaging

By

Archer Elleen Chattin

Thesis

Submitted to the Faculty of the

Graduate School of Vanderbilt University

in partial fulfillment of the requirements

for the degree of

MASTER OF SCIENCE

in

Earth and Environmental Sciences

August, 2015

Nashville, Tennessee

Approved:

Professor Guilherme A. R. Gualda

Professor Calvin F. Miller

To my cats, because dedications make me uncomfortable.

ACKNOWLEDGEMENTS

There are so many people who deserve to be recognized for helping me make this thesis and getting this degree possible. My mom, who had me reading by the time I was three years old and my brother who I always wanted to keep up with. My sister-in-law, Amanda, who kept my spirits high and was always around to listen. I would like to acknowledge all the fantastic teachers I had in elementary through high school who never told me I couldn't be a scientist. In college I had wonderful professors that encouraged me to continue even though I was a minority. Tom Lehman, Aaron Yoshinobu, and Calvin Barnes all helped me be an excellent student and worker. They gave me the courage to keep going even when I was overwhelmed. These professors encouraged me to branch out, leave my comfort zone and accept a place at Vanderbilt University. Here at Vanderbilt I have had the pleasure of meeting incredible, inspiring professors, peers, and students. A special thank you is deserved by Tami Gray, David Fry, and Trina Merrick for helping me remember calculus, offering a safe place to vent, and making sure my days weren't just work, but also enjoyable. My advisor Guil Gualda gave me the opportunity to learn new skills and applications and along with the other members of my master's committee, Malu Jorge and Calvin Miller, kept me focused on my goal. Thank you to Jim Gardner for his excellent experimental work, and David Furbish for his mathematical brilliance and patience. Ayla Pamukcu was my go-to for when things weren't going as planned and she always knew how to help when others wouldn't. Finally I would like to acknowledge the rest of the EES graduate students and faculty, the office staff, the Vanderbilt community as a whole and, of course my two cats Neo and Trinity who have kept my stress level down and always know when to sit on the keyboard and signal that I've worked enough for one day.

TABLE OF CONTENTS

PART I

DECOMPRESSION RATE AND ITS EFFECT ON CRYSTAL GROWTH

PART II

DETERMINATION OF VESICLE SIZE DISTRIBUTIONSUSING X-RAY TOMOGRAPHY

LIST OF TABLES

PART I

PART II

LIST OF FIGURES

PART I

PART II

INTRODUCTION

Supereruptions

Volcanic eruptions are among the most fascinating and publicly accessible geologic phenomena. Eruptions are terrible, beautiful, and an issue that parts of the United States have to consider and plan for as a possible threat to safety and property. Significant time, energy, and research dollars have been spent to understand the timing, triggers, properties, and processes of volcanic eruptions in order to better predict and understand these eruptions. Though this is a relatively straightforward task when considering eruptions like those in Hawaii and Washington, eruptions that happen relatively frequently and eject less than a cubic kilometer of tephra or lava, it is impossible to complete by normal methods of observation and study for infrequent eruptions of enormous magnitude, such as those at Yellowstone and the Long Valley Caldera. These eruptions are known as supereruptions, explosive silicic eruptions that expel at least 450 km^3 of material and have a volcanic explosivity index (VEI) of 8 or higher (Miller and Wark 2008, Francis and Oppenheimer 2004).

Supereruptions occur so infrequently-- the youngest being the Oruanui eruption in New Zealand 26,000 years ago (Wilson 2001) -- that the scientific community has never had the opportunity to witness the event. Their rarity and massive size suggest the possibility of differences in growth, storage, and/or eruption from their smaller counterparts. As a result, the only sources of information on the lead-up and eruption of these colossal systems are the deposits left behind by previous eruptions. Due to this limit in reference sources, those of us

who study the syn-eruptive timing and processes of supereruptions are tasked with finding new ways to understand and interpret the limited data we have. These deposits contain compositional and textural features that have recorded processes that took place before and during eruption, providing evidence of that which we cannot experience firsthand (Hildreth 1979, Gualda and Ghiorso 2013, Hervig and Dunbar 1992, Pamukcu et al 2012). The processes leading to and facilitating supereruptions are of great interest to the scientific community (Gualda et al 2012, Pamukcu et al 2012, Wallace et al. 1995, Wark et al. 2007, Gualda and Ghiorso 2013) as changes in crystallinity and bubble content during decompression and the lead-up to eruption may hold important information on rate and timing of supereruption events (Pamukcu 2012, Cashman 1992, Gualda et al. 2004). This study seeks to employ and refine two approaches to mining data from existing samples in order to expand the body of knowledge of syn-eruptive processes associated with supereruptions. Method one consists of using a scanning electron microscope and decompression experiments to replicate the conditions and timescales of decompression as evidenced by textures and crystal assemblage. Method two uses tomographic image analysis to investigate the vesicle size distributions of late erupted Bishop Tuff units and note any changes in vesiculation over the course of eruption.

The Bishop Tuff

The Bishop Tuff is a rhyolitic eruptive unit composed of both ash fall and ignimbrite deposits emplaced 0.76 million years ago over an estimated six day period of collapse of the Long Valley Caldera in eastern California (Hildreth 1979, Bailey et al. 1976, Wilson and Hildreth 1997). The Caldera is located between the Sierra Nevada and White Mountains just south of

Mono Basin (Figure 1). Though the Long Valley system is responsible for more than 200 eruptions throughout history, the Bishop Tuff supereruption is by far the largest erupting at least 1000 cubic kilometers of material (Hildreth and Wilson 2007, Bailey et al. 1976). Bishop Tuff deposits are concentrated in the areas to the northwest and southeast of the caldera (see Fig. 1) though significant ashfall is seen as far east as Nebraska (Hildreth and Wilson 2007).

Interpretation of stratigraphic relationships has led to the conclusion that the eruption was short-lived and largely continuous, lasting around 125 hours (Wilson and Hildreth 1997), though the magma body itself is thought to have existed for much longer before eruption. The duration of magma storage for the Bishop Tuff has been estimated several times over the years, with older estimations suggesting timescales of 100 ka or more (Simon and Reid 2005**)** and more recent ones giving much shorter timescales on the order of a few thousand years (Gualda et al. 2012, Crowley et al. 2007). Petrologic investigation of the Bishop Tuff yields evidence that the early-erupted Bishop Tuff is relatively crystal poor while the late erupted deposits are crystal-rich, containing ~30% crystals including phenocrysts of quartz, plagioclase, sanidine, biotite and iron-titanium oxides (Gilbert 1938, Bailey et al. 1976, Hildreth and Wilson 2007, Hildreth 1979, Wilson and Hildreth 1997, Gualda et al. 2004, Pamukcu et al. 2012, Wallace et al. 1999, Anderson et al. 2000). The source of this compositional difference is still being investigated, most recently by Gualda and Ghiorso (2013) who reject the “standard”, prevailing theory of a stably stratified crystal mush (Hildreth 1979, Hildreth and Wilson 2007) in favor of two separate, laterally juxtaposed bodies.

Though significant study has been previously conducted in areas including pre-eruptive storage (Hildreth 1979), geochemistry (Wilson and Hildreth 1997, Hildreth and Wilson 2007), crystallization history (Pamukcu et al. 2012, Gualda et al. 2012, Gualda 2007), and bubble populations (Gualda 2007, Gualda et al. 2004, Gualda and Anderson 2007) controversies still exist concerning the models of magma storage (Hildreth 1979, Wilson and Hildreth 1977, Bailey 1976, Gualda and Ghiorso 2013), the timescales of storage (Simon and Reid 2005 Gualda et al 2012, Gualda and Ghiorso 2013), crystallization (Simon and Reid 2005, Crowley et al. 2007, Gualda et al. 2012, Pamukcu et al. 2012), and the specifics associated with the transition from stable to eruptible material (Pamukcu et al 2012, Gualda et al 2012, Gualda 2007, Gualda et al. 2004, Wallace et al. 1995, Wark et al. 2007). With this study I hope to add relevant data to the discussion specifically concerning bubble populations, syn-eruptive crystallization, and timing of eruption-associated processes such as decompression.

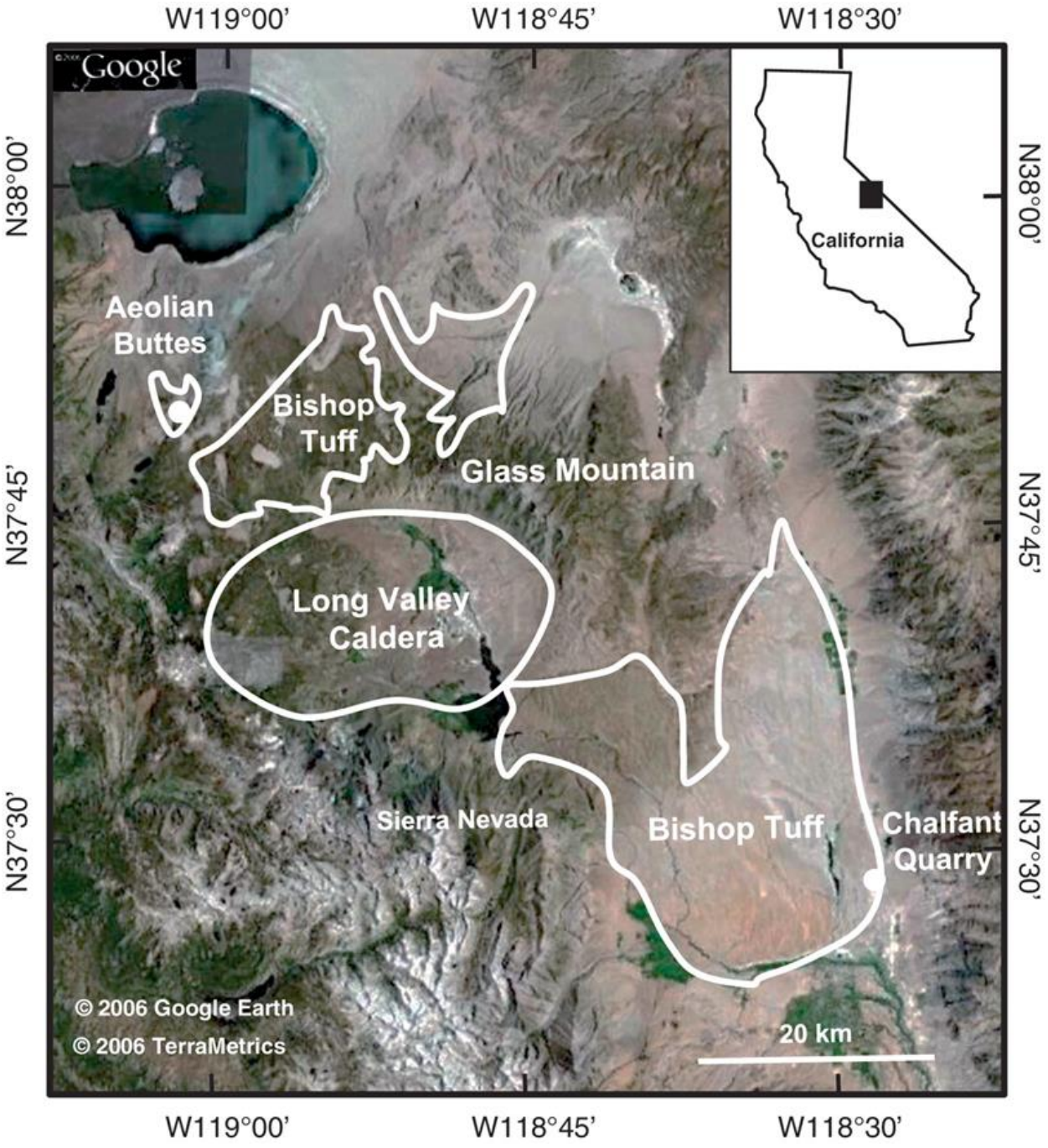

Figure 1. Map of Bishop Tuff deposits and surrounding area from Pamukcu et al. 2012.

PART I

DECOMPRESSION RATE AND ITS EFFECT ON SYN-ERUPTIVE CRYSTAL GROWTH

CHAPTER I

INTRODUCTION

Two distinct evolution phases in the late-erupted Bishop Tuff have been identified by Pamukcu et al. (2012) (Figure 2). The first phase is dominated by significant crystal growth over time periods of as much as 5000 years. This phase is characterized by low nucleation rates and growth of sizeable quartz, >50 µm, plagioclase, sanidine, and Fe-Ti oxide phenocrysts. The second phase is characterized by sudden rapid new crystal nucleation taking place over no

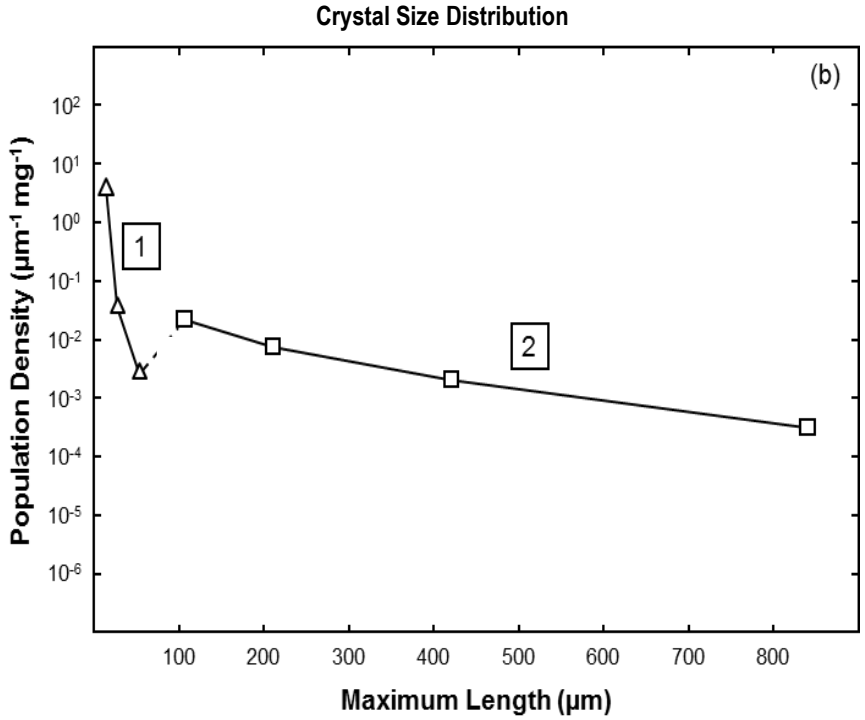

Figure 2. Example Crystal Size Distribution for the Bishop Tuff. (1) Corresponds with syn-eruptive crystals <50 µm in length. (2) Corresponds to pre-eruptive crystals grown over ~5000 years. (Modified from Pamukcu *et al.* 2012)

more than 1-2 years, resulting in a significant population of quartz and feldspar microlites 50 µm or less in size. The small size of these microlite crystals made the population difficult to

identify by normal methods such as petrographic microscopy and was recognized only after x-ray tomography of the material allowed analysis of a large volume of material at high resolution. Pamukcu et al. (2012) associated the second growth stage with syn-eruptive decompression of the magma while the first phase of crystal growth was considered pre-eruptive. Assuming Pamukcu et al. (2012) are correct, the microlites' textures and compositions are a direct, unique result of decompression rate during eruption. By studying these microlites in more detail and analyzing their counterparts in a set of decompression experiments I will investigate the effect of decompression rate on microlite crystal growth and overall pumice texture.

CHAPTER II

METHODS

Using glass inclusion compositions projected in the fashion of Blundy and Cashman (2001) in combination with Rhyolite-MELTS simulation results, Gualda and Ghiorso (2013) are able to come up with reasonable pressure estimates for early- and late-erupted Bishop Tuff. Knowing a general pressure range, composition, and final crystal population from previous study, we propose that obtaining a logical estimation of decompression rate becomes a matter of experimental trial and error.

Magma Recreation and Decompression Experiments

Preparation of materials and the decompression experiments themselves were run by James Gardner and his associates at the University of Texas at Austin. To insure the compositions of his experiments were as close to the natural composition as possible the experimental material was created by crushing Bishop Tuff sample AB6202 into a fine powder and then melting the material in the presence of enough water to recreate water-saturated conditions. The choice to assume water saturated conditions was based on work establishing fluid saturation for the early erupted Bishop Tuff based on glass inclusion analysis and investigation of a suspected pre-eruptive bubble (Wallace et al. 1995, Wallace et al. 1999, Anderson et al. 2000, Gualda and Anderson 2007). The fluid saturation of the late-erupted Bishop Tuff is less well established due to lower water and higher CO_2 concentrations in glass inclusions, however syn-eruptive crystallization in fluid-unsaturated conditions would have

been difficult. Once the sample magma was created it was loaded into a pressure capsule at 130 MPa. The capsules remained at 130 MPa for 97 hours to create G1283, the 'starting material' with which all experiments began. For each trial G1283 was decompressed from 130 MPa to 10 MPa. The rate of decompression and the temperature at which it occurred were varied between experiments in an effort to find the conditions that most closely recreate those of the Bishop Tuff eruption. Pamukcu *et al.* (2012) concluded that syn-eruptive crystals grew in no more than 1-2 years. Based on the stratigraphically estimated eruption duration of 127 hours and the capabilities of the space and equipment available to us we chose to investigate the extent of decompression-driven effects over hours and days. And though such a short timeframe may or may not capture the entirety of crystal growth and texture changes associated with the actual eruption, we are operating under the assumption that some extent of identifiable textural and compositional changes would be visible after only hours or days of decompression. Seven decompression experiments were conducted (G1288, G1287, G1289, G1366, G1381, G1418, and G1419), each with a unique combination of starting temperature and decompression rate; these are listed in Table 1. All experiments were isothermal.

	20 MPa/hr	5.5 MPa/hr	1.7 MPa/hr	0.75 MPa/hr	Static
710°C	G1288	G1287	G1366	G1419	
785°C		G1289	G1381	G1418	
750°C					G1283

Table 1. Temperature and decompression rate associated with experimental trials. Decompressions were isothermal.

Sample Preparation

All products from the decompression experiments were brought to Vanderbilt University upon the conclusion of their decompression and were prepared for use in the Scanning Electron Microscope. I mounted the materials in one-inch epoxy mounts then ground and polished each mount with decreasing grit diamond suspensions on a Buehler Ecomet grinder/polisher. Once polished, I coated the mounts with carbon using a Q150T Turbo-pumped carbon coater.

Crystal Population Analysis

Scanning Electron Microscope (SEM)

Though the presence of microlite quartz + feldspar crystals in late-erupted Bishop Tuff has been established by Pamukcu *et al.* (2012) in high resolution in 3D, use of x-ray tomography for the present study was impractical. Instead we chose to study experimental products using SEM imaging. By using resources readily available to me I can pre-analyze samples, identify syn-eruptive growth markers, and assess which samples would be valuable candidates for tomographic imaging later on.

The Tescan Vega 3 Scanning Electron Microscope (SEM) at Vanderbilt University was used to characterize the textures and crystal assemblages of all experimental products along with a selection of pumice samples from late-erupted Bishop Tuff samples AB6202, AB6201, and AB5301. Back-scattered electron (BSE) images were collected for general classification of phenocrysts and textures as well as for comparison of experimental results to natural Bishop

Tuff crystal populations. In conjunction with the SEM, an Oxford X-max 50mm^2 energy dispersive X-ray spectrometer (EDS) and Aztec software were used to obtain standardless quantitative compositional information about glass, phenocrysts, and microlite crystals, both in natural and experimental material. Cathodoluminescence (CL) imaging was used to identify microlite quartz crystals too small or too similar in brightness to the glass in BSE images, as well as to verify the identification of quartz found in BSE and to see any compositional zoning present. CL and BSE maps were collected of AB6202 for further image analysis. Table 2 lists specific operating parameters.

SEM Operating Parameters	
Accelerating Voltage	11-20 kV
Beam Intensity	18-19
EDS x-rays collected	0-10 kV
Working Distance	15m

Table 2. Operating conditions used with the SEM to obtain images used for this study.

False Color Image Analysis

To intensify the visual difference between quartz and glass in CL and BSE images and make locating quartz microlites more efficient I changed the color values associated with each brightness range so that the contrast between them would be easier to spot. The brightness values assigned to pixels making up quartz phenocrysts in the original black and white images were extracted in Matlab. CL images were first thresholded to remove high intensity noise and then, using Matlab software, I applied a color map with custom RGB intensities. The values

chosen to represent quartz were as far removed as possible on the color wheel from that of glass (Figure 3a-b).

BSE images were converted into color images in which all 3 color channels contained identical color value information, copied from the original black and white image. A grayscale copy of the images was thresholded so that all color values in the image were set to zero except those associated with quartz phenocrysts. The brightness values of the thresholded image were then added to values already in the red color channel of the original image, intensifying the brightness of pixels in that channel that overlap with the pixels in the thresholded image. Because this added brightness only exists in the red color channel, these pixels will show up with a red tint while the rest of the image remains grayscale (Figure 3c).

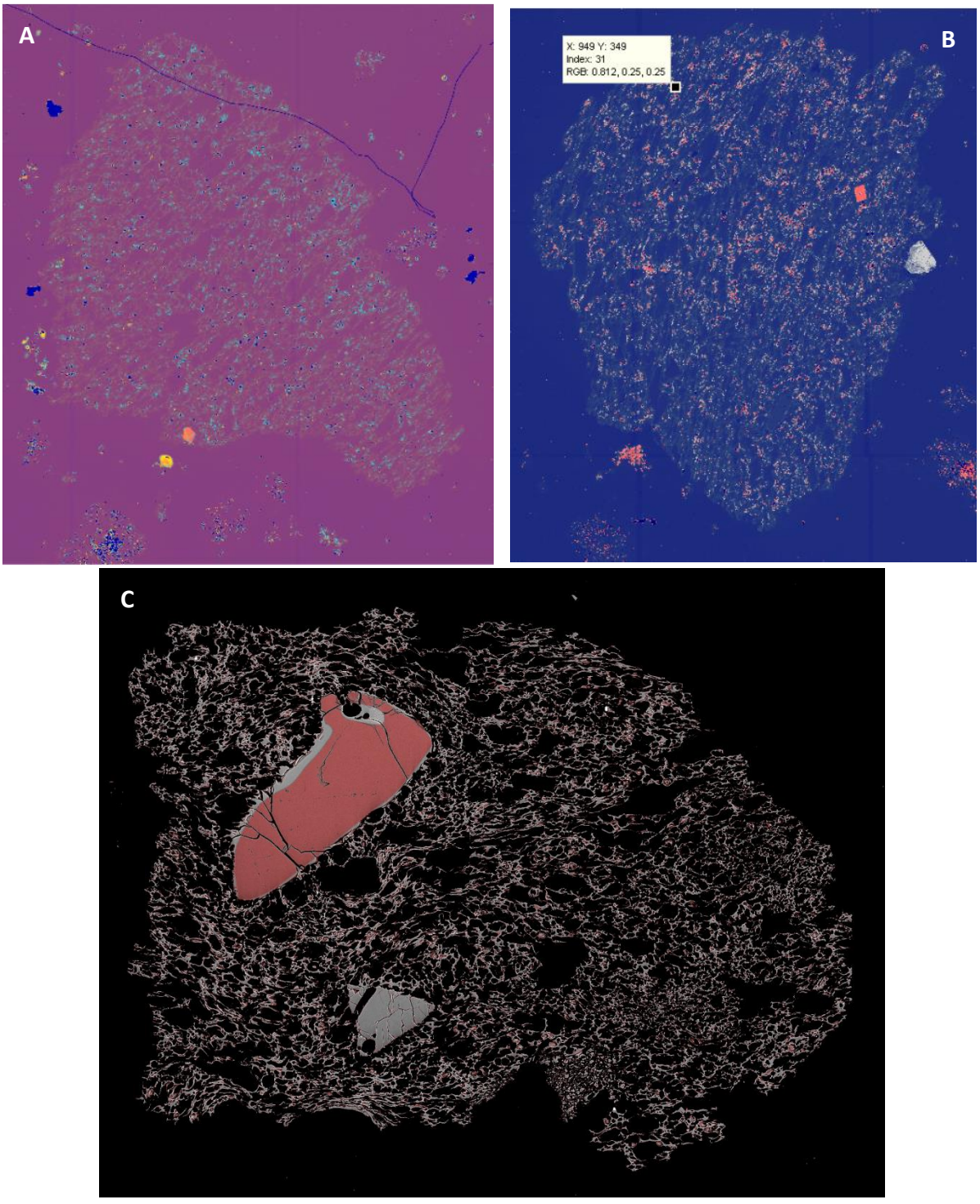

Figure 3. a) Color mapped pumice clast. Image is thresholded to remove noise, and then color map applied. Bright orange-pink indicates possible quartz. b) A separate color mapped clast. Colors vary due to a difference in original image intensity. c) Pumice clast with quartz-indicative color values intensified in the red channel.

CHAPTER III

RESULTS

Natural Bishop Tuff

To establish a baseline for the crystal characteristics and textures indicative of conditions in place at the time of the Bishop eruption, I documented textures of natural late-erupted Bishop Tuff Pumice samples AB6202, AB6203, and AB5301. The natural material is highly vesiculated; AB6202 and AB5301 have a majority of equant bubbles while AB6203 contains large areas where the bubbles have become elongated (Figure 4). Phenocrysts are as large as 800 µm in length and as small as 2-3 µm. Phenocrysts include quartz, plagioclase, sanidine, biotite, pyroxene, and iron-titanium oxides (Figure 5 a-b). AB5301 also contains sparse monazite crystals, 20-35 µm in length and pyroxene (Figure 5 c-d).

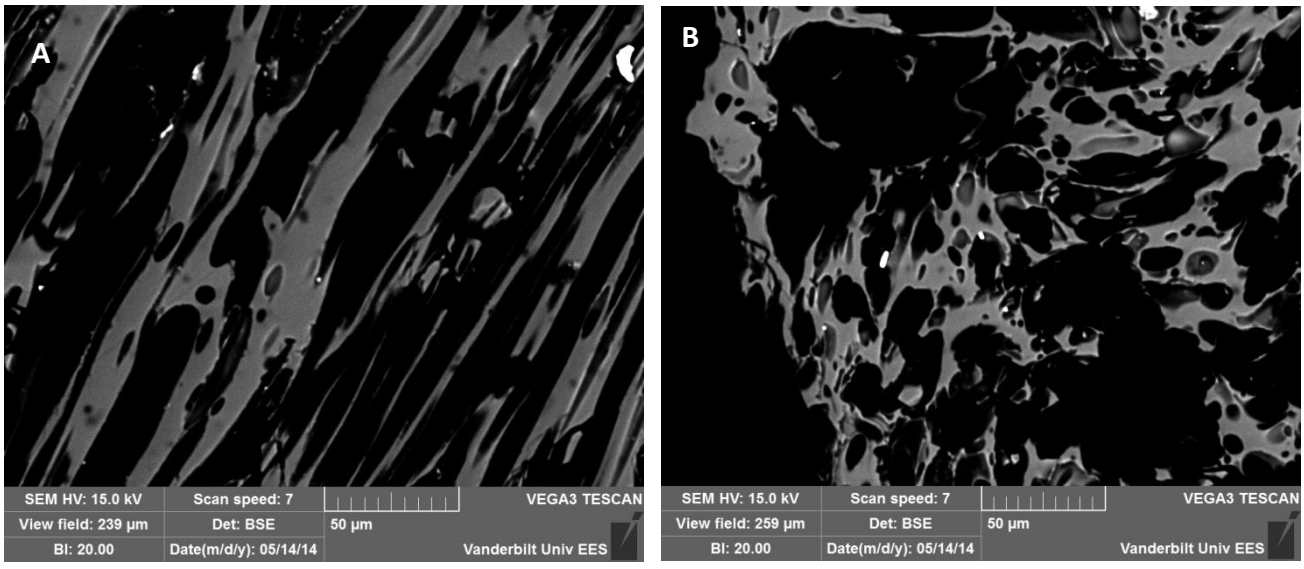

Figure 4. Comparison of bubble shapes between Bishop samples. a) A close-up of AB6203 showing elongate bubble shapes. b) Close up of Ab 5301 showing more rounded, equant bubble shapes.

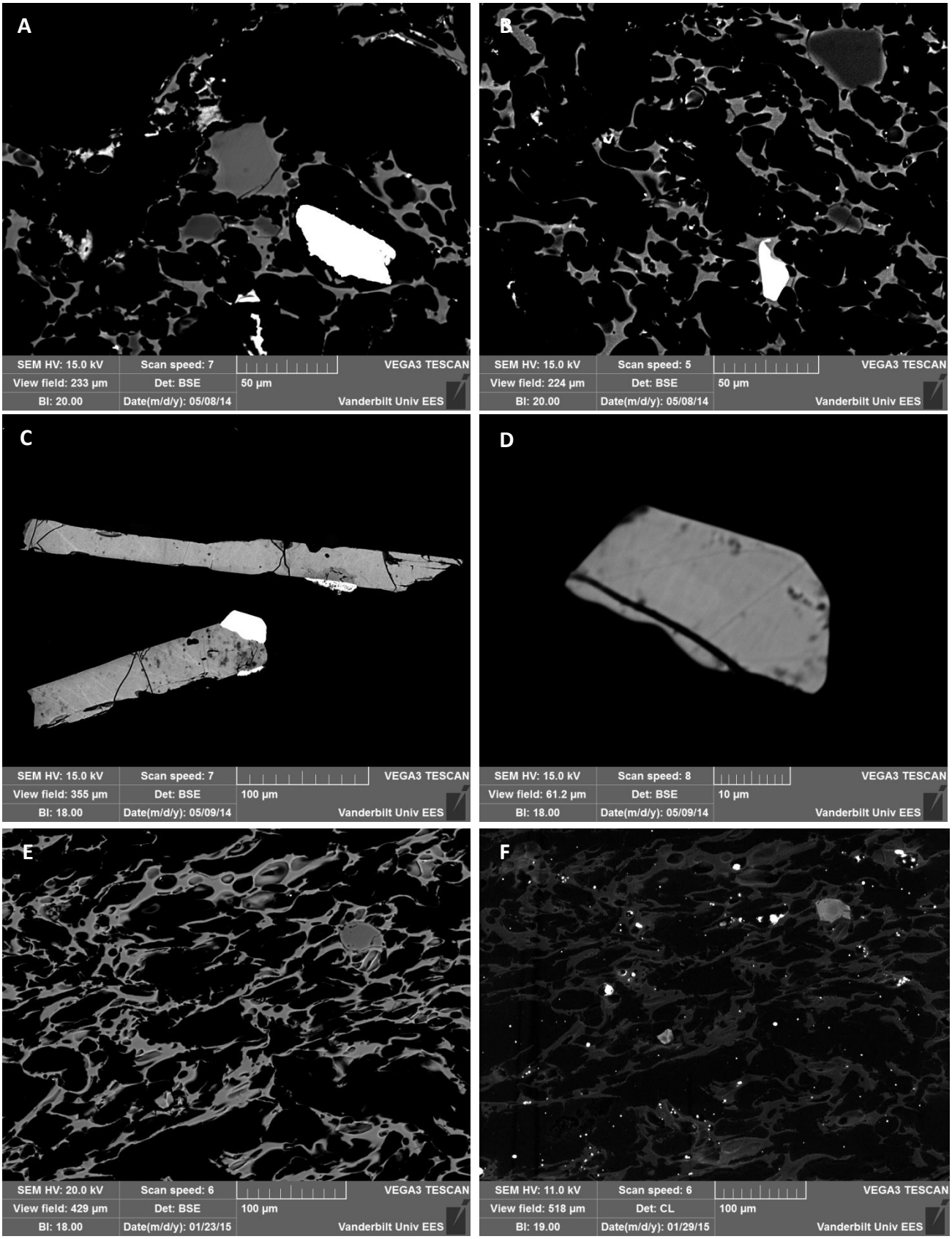

Figure 5. Crystals in natural Bishop Tuff samples. A) Backscatter image of quartz, sanidine, and oxides in AB6202. B) Quartz and oxides in AB6203. C) Backscatter image of pyroxene and monazite in AB5301. D)Detailed backscatter image of monazite in AB5301. E-F) Quartz microlite in backscatter (E) and CL (F).

Syn-eruptive quartz microlite crystals as identified by Pamukcu et al. 2012 were few in number, but present in all three samples. Each mounted sample afforded me ~ 0.0001 cm^3 of material to analyze and contained between 5 and 20 microlite quartz crystals 2-50 µm in size. This is consistent with the number of microlites we expected to see based on the number density of microlites per cubic centimeter identified through tomography which is 100,000 or 10 for a sample equal in volume to ours. These microlite quartz crystals are sub- to euhedral; a portion show dark cores with lighter rims in CL images while others contain no zoning (Figure 5 e-f). Quartz microlites were confirmed using EDS analysis.

Starting Material

Despite our efforts to completely melt the sample used as a starting material, SEM imaging shows that crystals remain (as they would have in the Bishop Tuff magma). Therefore, when the experimental products are analyzed I must take into consideration that not all of the crystals present are new and I need to develop a systematic way to identify pre-existing and newly grown crystals.

G1283 (Figure 6A) contains little to no vesiculation; vesicles that are present are isolated and <100 µm in size. Fragmented, irregular crystals of quartz, plagioclase, sanidine, biotite, iron-titanium oxides and other accessory phases are present throughout. Quartz 60-100 µm in size display jagged, irregular shapes and little to no zoning in CL images. Quartz crystals 100-150 µm in size display significant zoning truncated by broken edges in CL (Figure 6B) indicative of growth over long time periods and disruption in the process of creating G1283. Plagioclase crystals range in size from 50 to 300 µm. Sanidine spans an even larger range of sizes with

crystals 10-500 µm in length and in various states of breakage. Some sanidine crystals are fragmented into 2-3 pieces while others are shattered into dozens of splinters 50 µm or less. Biotite exists primarily as 10-50 µm undulating filaments showing cleavage planes, though some basal sections are present. Iron-titanium oxides and apatite <10 µm are scarce in number but found throughout the sample.

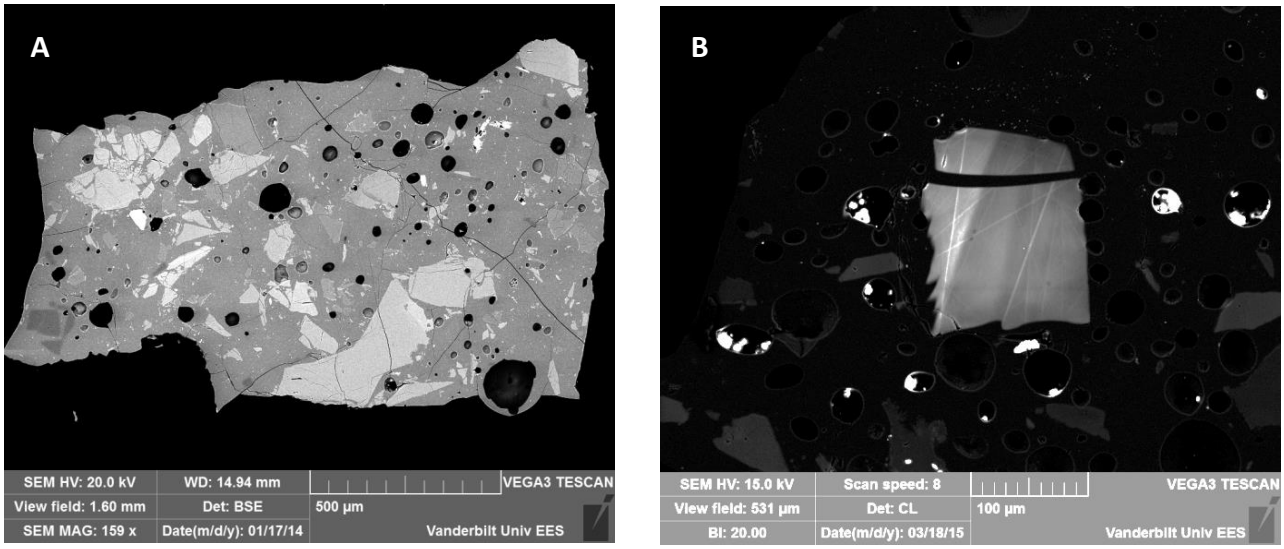

Figure 6. (A) Overview of starting material composition in BSE. Quartz shows as dark gray in bottom left corner, sanidine shows as light gray, the largest phenocryst, bottom center. Brightest white crystals are biotite, titanium oxides, and other accessory phases. (B) Example quartz phenocryst in CL revealing zoning that places this crystal as one part of a much larger whole at some point previous.

Experimental Products

The seven experimental products were divided into three categories based on the length of time they underwent decompression. These categories were as follows: short duration—less than 24 hours; mid-length— 3 days; and long duration—6 days. Each category yields a unique combination of products.

Short Duration Experiments

Three short duration experiments were carried out, G1287, G1288, and G1289, the conditions of which are listed in table 1. Short duration experiments are highly vesiculated relative to the starting material (Figure 7 A-C). Phenocrysts 200-300 µm in length of plagioclase, and sanidine are present in all three short duration experimental products; 200-300 µm quartz crystals are present in G1287 and G1288, but none are present in the sample volume available to be imaged for G1289. Small oxides, 10-20 µm, and accessory phases are also present in all three categories of experimental products.

Crystals, especially of sanidine, have been broken and fragmented during decompression (Figure 7F) complicating the process of identification of new growth. In relatively crystal-free areas an abundance of euhedral 2-10 µm sanidine and biotite microlites is seen (Figure 7d). Reaction rims in BSE that are non-luminescent in CL images are found around a majority of quartz phenocrysts in both G1287 and G1288.

Mid-length Experiments

Two mid-length experiments were carried out, G1366 and G1381, each lasting close to 3 days. Both G1366 and 1381 are vesiculated and contain a larger number of bubbles than the starting material, but fewer and larger bubbles than are seen in the short duration experiments (Figure 8A-B). Quartz, sanidine, and plagioclase phenochrysts 100-400 µm are present in both experimental products. Biotite, monazite, and other accessory phases are also present at sizes

100 µm or less. Significant sanidine growth has taken place over the course of the three-day decompression, both in the form of newly nucleated, independent laths (Figure 8C) and as 3-5 µm thick rims around phenocrysts (Figure 8D). Notably, sanidine rims have grown around not only pre-existing sanidine phenocrysts but also around plagioclase and quartz (Figure 8D). The rims are jagged and vary in thickness around individual crystals. On other quartz crystals there are bright rims in BSE that are uniform in thickness but that do not appear luminescent in CL images (Figure 8E-F). Fragmentation of crystals has taken place but not to the extent seen in the short duration experiments.

Long Duration Experiments

Two long duration experiments have been carried out. G1418 and G1419 were decompressed over 6 days, the slowest decompression rate investigated thus far. Relative to one another, the high temperature, long duration experiment G1418 yielded cleaner products with less new crystal nucleation while G1419 has little crystal-free glass and an abundance of sanidine laths 2-10 µm in size and biotite microlites <2 µm. Both G1418 and G1419 are vesiculated, though poorly. Each experiment appears to have maintained the crystals inherited from the starting material largely intact, including fragments of large quartz that show truncated zoning (Figure 9A). G1418 contains sanidine growth rims around a portion of its crystals, though the rims are not as thick or prominent as those seen in the mid-length trials. At least one microlite quartz < 5 µm in length was identified in G1418 (Figure 9B). Small, irregularly formed quartz crystals 10 -40 µm in size are present throughout sample G1418. These crystals are bright in CL images except for a dark core at the centers (Figure 9C, E-F).

G1419 also contains a few of these irregular quartz microlites. In addition, G1419 contains 100-300 μm quartz crystals with thin, bright, irregular thickness rims in CL images (Figure 9 E-F) as well as irregular quartz that has grown interstitially between sanidine laths (Figure 9D).

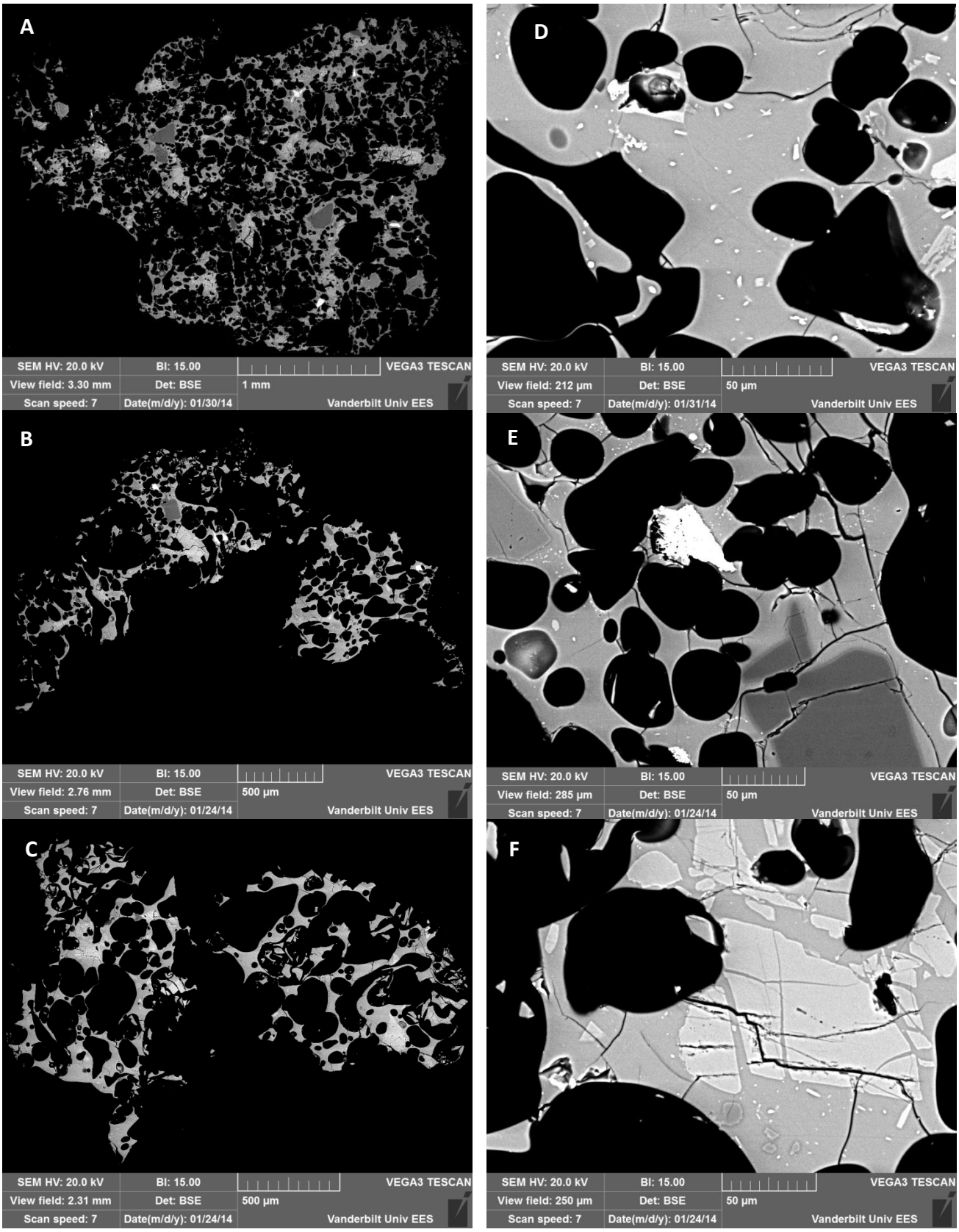

Figure 7. (A-C) BSE overview image of G1287, G1288, and G1289 respectively, short duration experiments with significant vesiculation and persisting phenocrysts 200-300 µm in size. (D) BSE of sanidine lath growth in G1287. (E) BSE image of quartz reaction rims in G1288. (F) BSE image of sanidine phenocryst fracturing and splintering.

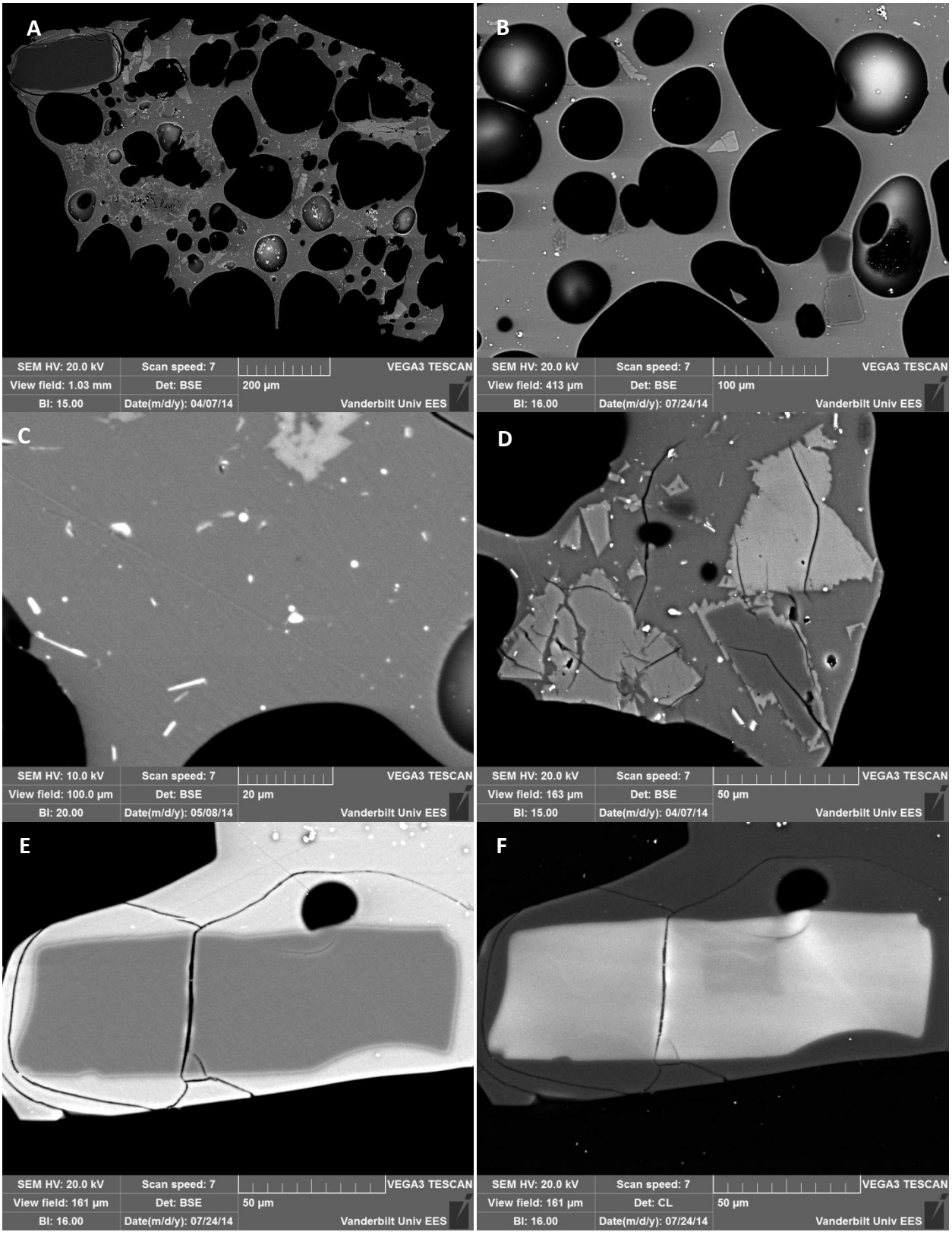

Figure 8. (A) Overview of G1366 phenocryst assemblage and vesiculation. (B) Detail BSE image of G1381 vesiculation and quartz, plagioclase, and sanidine crystals. (C) BSE image of sanidine lath growth in G1366. (D) Area of significant sanidine growth as rims around quartz and sanidine phenocrysts. (E-F) BSE and CL images respectively of quartz in G1381. Reaction rim in E does not translate to F.

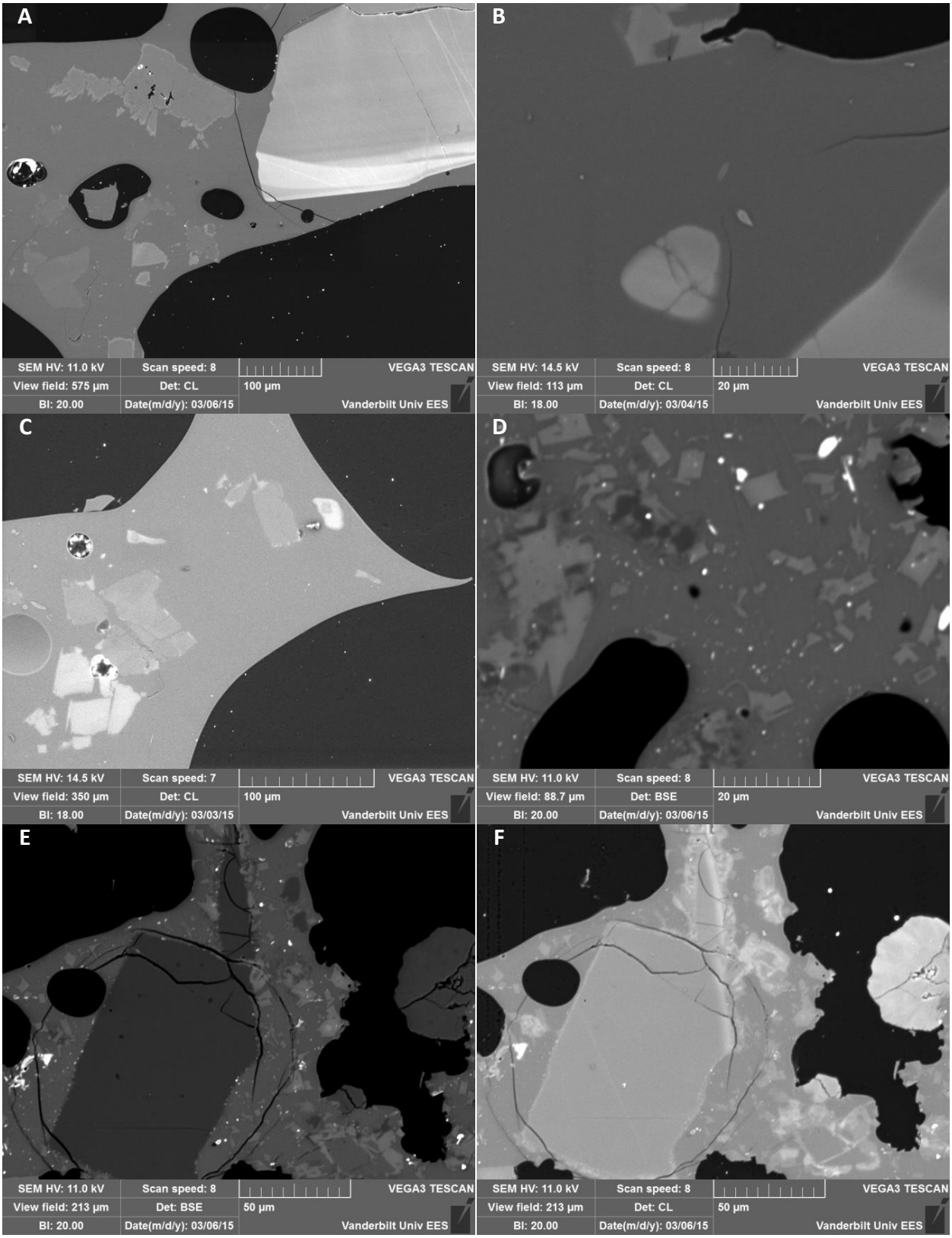

Figure 9. (A) Relict quartz in G1418 in CL. (B) CL image of G1418 quartz, including a 1-2 µm microlite. (C) CL image of quartz in G1418, upper left, have dark cores and light rims. (D) Significant sanidine growth and interstitial quartz. (E-F) BSE (E) and CL (F) images of quartz in G1491. Rims in F suggest new growth.

CHAPTER IV

DISCUSSION

The textural differences between natural Bishop Tuff pumice chips and short-, mid-, and long-duration decompression experimental products provides unique insight into the conditions and processes associated with the Bishop Tuff magma system in the midst of eruption, as well as syn-eruptive processes of supereruptions in general. Size and presence of quartz microlite crystals in different length experiments helps to constrain the length and conditions of decompression needed to develop the crystal size distributions identified by Pamukcu *et al*. (2012). The extent of vesiculation varies within experimental products and gives a sense of the decompression rate associated with bubble nucleation and growth.

Syn-Eruptive Crystal Growth During The Bishop Tuff Eruption

Natural Bishop Tuff

Quartz microlites found in each of the three natural pumice clasts displayed a variety of characteristics that are indicative of new crystal growth during decompression. The first of these characteristics is the bright rim formed around a dark quartz core in CL images. The change in intensity between different zones in quartz under CL is an indication of a change in composition during crystal growth (Gualda et al. 2012, Matthews et al. 2012). In this case that change is attributed to degassing and rapid change of the crystallization regime from slow and steady over thousands of years to sudden and rapid crystallization over days or months.

The second attribute observed in a majority of natural Bishop Tuff quartz microlites is the prevalence of rounded edges and/or space-filling shapes rather than sharp corners. This is due to the fact that quartz microlites are new and unbroken. In addition, syn-eruptive crystals are growing interspersed with pre-existing crystals and therefore may be limited on space and unable to express their euhedral form when growing in close proximity to other crystals. The consistent presence of these characteristics in all three samples makes it likely that we may use such characteristics as an indication that quartz crystals displaying these characteristics in the experimental products are from decompression-driven growth.

Experimental Products

Each of the three groups of experiment length described above contains different assemblages of crystal sizes and textures. This gives credence to the hypothesis that the growth of crystals and final textures seen in pumice clasts from supereruptions are significantly impacted by changes in conditions of storage and movement associated with the process of eruption. It also allows us to estimate the timescales over which decompression-driven growth of crystals and bubbles takes place.

New growth in short duration experiments appears to be restricted to sanidine and biotite, and even then growth is limited and short-lived judging by the lack of sanidine rims on pre-existing crystals and a maximum size of 3-4 μm for newly grown microlites. Quartz reaction rims identified in figure 7E are likely evidence of a hatius in quartz crystallization during syn-eruptive decompression rather than a sudden nucleation event. Fragmentation of pre-existing crystals, while often taken as evidence of a pause in crystallization, are of little to no

consequence in this situation considering the sample's history of reworking previous to the onset of final decompression experiments during the creation of starting material.

Mid-length experiments are characterized by considerable new crystal growth as a result of decompression. The sanidine rims seen in Figure 8D suggest that the length of time was sufficient and conditions of decompression were suitable during the mid-length experiments to facilitate sanidine growth since they do not exist in the starting material and exhibit euhedral crystal habit. However, the fact that thick sanidine rims grew not only around feldspar phenocrysts but also around quartz suggests that the conditions were not favorable for quartz growth, since the most likely location we would see that growth would be as rims around existing quartz crystals. Quartz crystals that lack sanidine rims have thin reaction rims like those seen in the short-duration experiments, another indication that quartz did not grow in the mid-length experiments.

Long-duration experiments appear to contain the first examples of decompression-driven quartz crystal growth as evidenced by thick bright rims around large quartz phenocrysts in CL images as well as 10-50 μm, rounded quartz microlites with dark cores in CL and interstitially grown quartz, all seen in Figure 9. The characteristics used to identify newly grown quartz in the long-duration experiments are similar to those used to identify quartz microlites in the natural Bishop Tuff pumice. This suggests that it is likely the newly grown quartz crystals in the experimental products correspond to the microlites in the natural material and that the conditions needed to produce these crystals in the experiments are within the realm of possible conditions in place during the eruption of the Bishop Tuff magma.

Decompression Rate And Bubble Nucleation

Like microlite growth, bubble nucleation and growth is a process influenced by decompression rate. Differences between the vesiculation of experimental products suggests there is a link between the extent of vesiculation that occurs during eruption and the rate at which decompression takes place in the system (Gardner et al. 1999, Larsen et al. 2004, Mangan and Cashman 1993).

The short-duration experiments are highly vesiculated with a high nucleation density as well as a variety of bubble sizes including bubbles 10 µm or less. This means supersaturation was high enough to lead to high nucleation rates and development of a population of small bubbles within the 6-22 hour experiments. However, the long-duration experiments are not well vesiculated and contain few bubbles 10 µm or less. Though these experiments should be long enough to produce both a large-bubble population and a small-bubble population, the latter does not develop, and thus it may be concluded that the slower rate of decompression is not conducive to triggering a sudden, high nucleation period such as that in the short-duration experiments. The natural Bishop Tuff samples are highly vesiculated and contain both large and small vesicles, at even higher number densities than in the short duration experiments, suggesting that the decompression rate needed to produce the bubble population seen in the Bishop Tuff was similar to or even faster than that used to produce the short-duration experiments.

CHAPTER V

CONCLUSIONS

Differences between the results of short-, mid-, and long-duration time frames are significant and present patterns that give us insight into the syn-eruptive processes taking place within the Bishop Tuff. Newly grown, syn-eruptive quartz crystals like those identified by Pamukcu et al. (2012) can be found in the natural Bishop Tuff samples using SEM imaging. These syn-eruptive crystals are characterized, in general, by a size of 50 μm or less, a dark core and lighter rim in CL images, or simply as a rim or space-filling phase around pre-existing quartz or feldspar phenocrysts. Quartz crystals matching these characteristics are, as of now, only found in experimental products of long duration experiments, with decompression taking place over ~6 days. The lack of syn-eruptive quartz growth in shorter duration decompession experiments suggests that microlite formation in the Bishop tuff most likely took place over a few days or possibly weeks.

Though decompression rates needed for crystal growth are relatively slow within the scope of our experiments, the rate needed for bubble nucleation and growth appears to be inherently different. This conclusion is drawn from the lack of significant vesiculation present in the long-duration experimental products. There is, however, a significant bubble population present in the short duration experiments. This suggests that bubble nucleation and growth on a large scale requires much faster decompression rates than crystallization. Because both syn-eruptive crystal growth and syn-eruptive bubble nucleation and growth occurred during the Bishop Tuff eruption, as evidenced by natural pumice analysis, it can be assumed that at

different times during eruption, different decomression rates were active. Likely, as eruption carried on, the rate of decompression increased and the growth regime underwent a switch from crystal-growth dominated to bubble-growth dominated, leading to the natural pumice textures deposited.

PART II

DETERMINATION OF VESICLE SIZE DISTRIBUTIONS USING X-RAY TOMOGRAPHY

CHAPTER I

INTRODUCTION

Crystals are often studied in magmas for their continued growth during magma eruption and ability to record magmatic processes. Vesicles also grow and develop concurrently with crystals in an eruption (Armienti et al. 1994, Gardner et al. 1999, Larsen et al. 2004, Mangan et al. 1993) and, like crystals, have the potential to offer valuable insight into syn-eruptive dynamics by quantifying their end-result populations.

The processes of vesiculation within erupting magmas have been studied by several scientists (Sparks 1978, Wilson et al. 1980, Houghton and Wilson 1986, Wilson and Head 1981, Sparks and Brazier 1982, Gardner et al. 1999, Larsen et al. 2004, Mangan et al. 1993; among many others). Many of these studies conlcude that bubble growth rates are largely dependent on volatile content and the diffusion coefficients of the volatiles (Sparks 1978). As concluded in Part I of this work, bubble nucleation and growth are also actively influenced by decompression rate and to produce both the crystal population and bubble populations seen in the Bishop Tuff the decompression rate had to have fluctuated during eruption. This means that different units of the late-erupted Bishop Tuff may contain unique distributions of bubble sizes that might represent important aspects of syn-eruptive process as they progressed through the eruption (Hildreth and Wilson 2007, Wilson and hildreth 1997, Gardner et al. 1991).

CHAPTER II

METHODS

The purpose of this study is to begin quantifying bubble sizes in pumice clasts from different eruption phases. An overall difference in vesicularity between phases is simple enough to obtain by calculating the percentage of open space using the bulk density of pumice clasts, but the distribution of sizes for the bubbles that make up that vesicularity presents a unique set of challenges. The ideal, most accurate way to determine a size distribution would be to measure and count each individual vesicle. However, due to the coalescence and interconnectedness of bubbles in pumice clasts it is difficult, if not impossible, to accurately separate one bubble from another.

With the advent of detailed, non-destructive, 3D imaging techniques many of the challenges associated with quantifying bubble size fractions are now surmountable. In this study I used various methods of tomographic volume processing that use 3D images to determine volumes that can then be used for bulk density measurements. We hope to more accurately and quickly quantify bubble size distributions in pumice clasts.

Samples

The samples used come from five separate horizons of the Bishop Tuff deposit, encompassing both ash fall units and ignimbrite: fall units F7, F8, and F9; and ignimbrite units Ig1EB and Ig2NW, as designated by Wilson and Hildreth (1997). Samples whose label begins with 'Ig' and those beginning with 'F' numbered above 100 were collected by Guil Gualda.

Samples whose labels begin with 'AB' and those beginning with 'F' numbered below 100 were collected by Fred Anderson. All samples were then prepared and imaged by Guilherme Gualda in 2005.

Analytical Methods

X-ray Tomography

3D imaging has the potential to be an important component of vesicle texture analysis (Baker et al. 2012, Gualda et al. 2010, Voltolini et al. 2011, Gualda and Rivers 2006, Pamukcu and Gualda 2010). The vesicles in pumice cannot be physically separated from the sample as crystals can because the physical object itself, the gas bubble, is lost during eruption. What we are left with is a network of interconnected casts of where those bubbles used to be and not actual, physically bounded objects. Without 3D context, thin sections do not give a complete record of vesicle size, orientation, or relationship to other vesicles. X-ray tomography was chosen as our imaging method of choice because it offers a complete 3D picture of the samples without destroying them. In addition the output of tomographic imaging lends itself to being processed and analyzed using 3D image processing on a computer.

Five samples from each horizon have been collected and analyzed using the bending magnet beamline at GSECARS, in the Advanced Photon Source at Argonne National Laboratories (for details, see Gualda and Rivers 2006). The samples are imaged as cylinders of varying size cut from each pumice clast; the cylinders vary from as small as 1-2.5 mm^3 (1mm diameter), and as large as 700-800 mm^3 (10 mm diameter) for the lowest resolution samples (Figure 10). For each two-fold increase in resolution, an 8-fold decrease in volume is required

by the machine (Pamukcu et al. 2012, Pamukcu and Gualda 2010). Tomography data were collected for four different clast sizes/resolutions per sample, totaling ~100 tomographic volumes available for analysis. The tomographic volumes consist of 3D volume elements (voxels) each of which represent the linear attenuation coefficient (a function of mean atomic number and density) of that sample volume (for details, see Gualda and Rivers 2006).

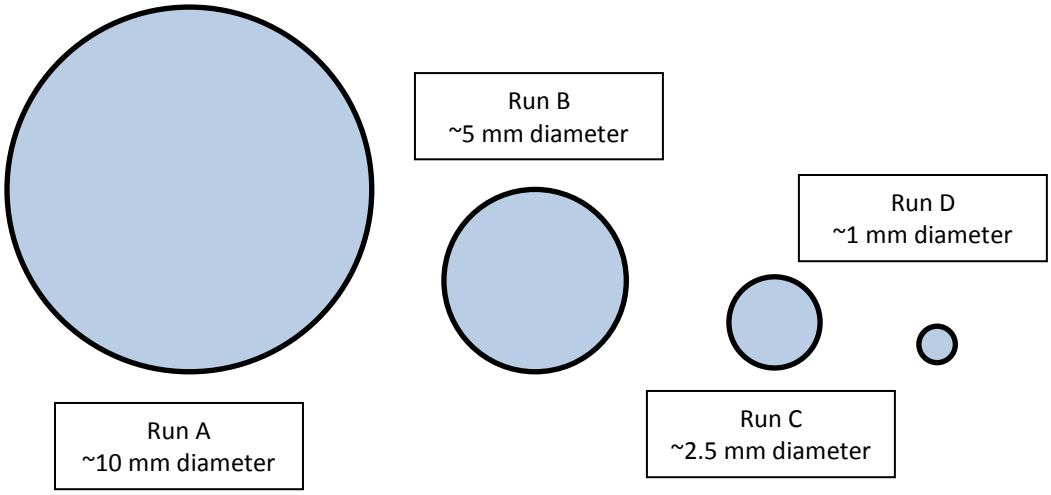

Figure 10. Schematic of relative sizes of pumice cylinders used for tomograpy

Volume Determinations

Our approach to determining vesicle size distributions is to determine the bulk vesicularity of each imaged pumice piece. We were careful to have our pumice pieces be fully enclosed in each 3D image (see Gualda & Rivers 2006, Pamukcu & Gualda, 2010), so that we could determine the bulk volume (by 3D image processing) and mass (using a precision scale). I used routines developed in our lab (using the IDL language) to quantify the volume of each imaged pumice piece. I used three different methods of image processing, one of which I developed over the course of this study.

For the first method, what we call convex hull, we digitally wrap the sample in the smallest possible convex 3D polyhedron that encompasses every pixel that represents glass or crystal, then count the number of voxels inside that polyhedron (Figure 11).

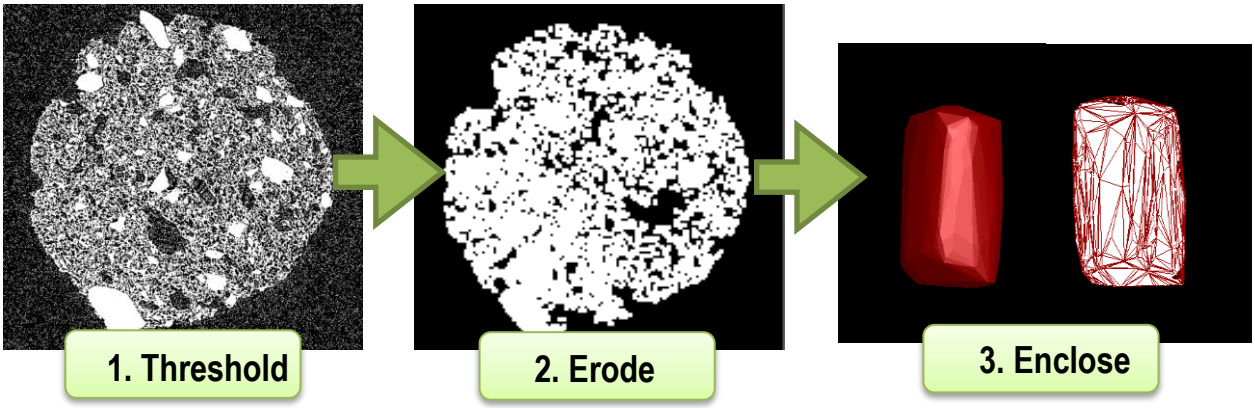

Figure 11. Representative slices in the z direction showing the image analysis preparation before running the convex hull command to generate the enveloping surface seen in 11.3

We used the methods and routines developed by Pamukcu et al. (2014) to perform the convex hull determination.

The second method, hereafter called morph close, uses a three-part process to fill in the black spaces that represent vesicles. First, the image is thresholded so that glass and crystals are white, and air (both vesicle and surrounding) is black. The value at which the image is thresholded is chosen to minimize the appearance of background noise as white voxels (Figure 12.1). In the second step a kernel, or element of a specified size, is used to determine a sampling area. This sampling area is then passed across the entire image voxel by voxel, eroding the image. In erosion the kernel is passed across the image and when the kernel origin (the center voxel) is occupied by a background voxel (a black voxel) all other voxels in the kernel area are converted to black pixels (Figure 12.2).

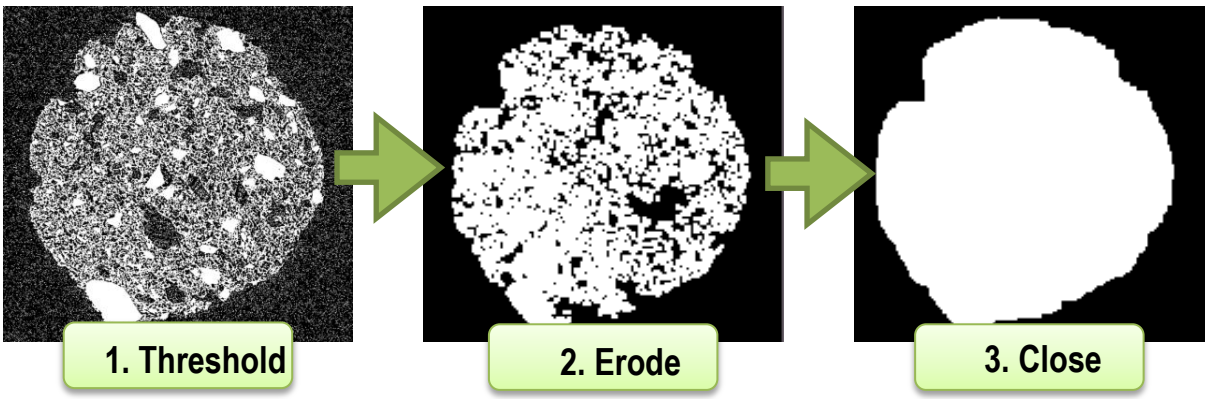

Figure 12. Representative slice through the z dimension showing the steps of the morph close volume determination method. 1. The image is thresholded to simplify the range of brightnesses. 2. The image is eroded to remove excess noise. 3. The image is dilated to fill in holes within the object boundaries.

The third step is to run the morph close operation, which is a combination of dilation (similar to erosion but emphasizing foreground--white voxels--rather than background) and subsequent erosion. By combining a dilation followed by an erosion, morph close is able to remove small background noise and fill holes smaller than the kernel area without needlessly increasing the overall size of the primary object by adding voxels to the perimeter as would happen in a

dilation alone. After the image has been processed, the sum of white voxels is determined and it corresponds to an estimate of the sample volume.

The third method I used (which I developed during the study), hereafter called perimeter difference, required that we again threshold and erode the image. We then count the number of voxels between the first and last white voxel on every row of voxels in the volume (Figure 13).

In this fashion, three independent volumes were digitally calculated for each individual sample by converting the number of voxels counted to cubic centimeters based on the image resolution and then these numbers were compared to identify any bias that may be present due to the method of analysis.

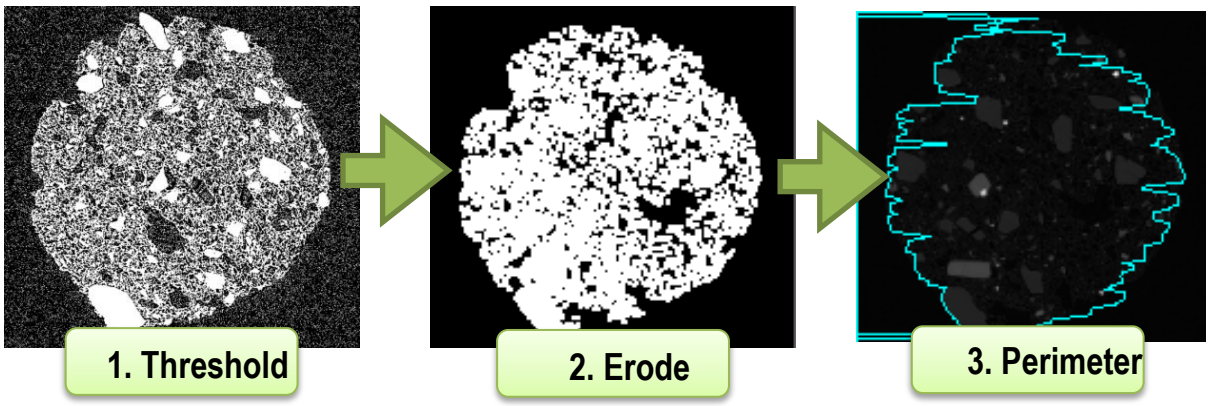

Figure 13. Representative slice through the z dimension showing the perimeter difference operation 1. The image is thresholded to simplify the range if brightnesses. 2. The image is eroded to remove noise. 3. The perimeter of the object is located and the number of pixels per row are counted and summed.

Bulk Density And Porosity Calculations

Measurements of bulk density were made for all samples and size fractions. Knowing the bulk density of our pumice clasts is imperative for calculating porosity and subsequently

vesicle size distributions. The mass of the sample gives us the mass of all the material contained within the volume of our sample. That volume, as we know, contains both the glass and crystals that the pumice is made of and the empty spaces within that represent the bubbles we are interested in. Because the bubbles are only casts and have no mass of their own we know that any mass factored into the density must be from glass or crystals and since the late erupted Bishop Tuff is known to be crystal-poor we assume the influence of crystals on the bulk density is minimal. By using the density of glass and the bulk density of the sample, the volume of glass necessary to cause that bulk density was calculated. That volume was subtracted from the total volume of the sample, and the remainder of the volume must be attributed to empty pore space representing bubbles.

Densities for clasts larger than 1cm in diameter were determined using a method based on Archimedes' principle described by Gualda (2007). In this method, clasts are weighed, then covered in silly putty and weighed again. The silly putty-covered clasts are placed in an apparatus that is suspended in water from a scale and can measure both positive and negative weights based on whether the clast floats or sinks. The silly putty is removed from the clast and its submerged weight is also determined. From these measurements, and the density of water, it is possible to determine the clast density (see Gualda et al. 2004 and Gualda 2007).

For clasts smaller than 1 cm diameter another method was developed because, for pieces smaller than that, the Archimedes method is not sensitive enough to capture the weight variations necessary to determine the density accurately. In this case the volumes calculated by tomogram analysis were used to calculate bulk density, ρ_B, using the following equation:

$$\rho_{B=}\frac{m_s}{v_s}$$

where m_s is the mass of the sample, collected previously by Guil Gualda and Ayla Pamukcu, and v_s is the volume calculated for the sample using the 3D image processes described above. The bulk density is then used to calculate the porosity percentage using ρ_g, the density of glass:

$$\%\ porosity = \left[1 - \left(\frac{\rho_B}{\rho_g}\right)\right] * 100$$

This calculation assumes that the only two things present are open space and glass with a density of 2.3 g/cm^3. This assumption is not true in most cases; crystals present in the pumice clast are generally denser than the glass and, if their presence is taken into account, would result in a smaller volume of physical material in the sample and a larger volume of vesicle space. To justify this assumption, we calculated the variation in porosity if we added the influence of crystals at different concentrations if they had a density of 2.7 g/cm^3 (Table 3). The

sample	Mass	Crystal volume			New porosity			Difference		
Ig_955		10%	20%	30%	10%	20%	30%	10%	20%	30%
A	0.216	0.0080	0.0160	0.0240	77.17	74.54	71.92	3.29	6.58	9.87
B	0.026	0.0010	0.0019	0.0029	77.37	74.77	72.16	3.26	6.51	9.77
C	0.005	0.0002	0.0004	0.0006	75.64	72.84	70.04	3.57	7.15	10.72
D	0.001	0.0000	0.0001	0.0001	70.56	67.18	63.79	4.58	9.16	13.74
AB_6202										
A	0.293	0.0108	0.0217	0.0325	69.19	65.65	62.11	4.87	9.74	14.62
B	0.033	0.0012	0.0024	0.0037	72.14	68.93	65.73	4.25	8.51	12.76
C	0.005	0.0002	0.0004	0.0006	74.58	71.65	68.73	3.77	7.55	11.32
D	0.001	0.0000	0.0001	0.0001	69.81	66.33	62.86	4.74	9.48	14.22
F	0.313	0.0116	0.0232	0.0348	68.29	64.64	60.99	5.07	10.14	15.21

Table 3. Crystal effect calculations for two of the study samples. The effect on porosity of adding 10%, 20%, and 30% crystals is shown and compared to the porosity calculated by ignoring the presence of crystals.

calculations demonstrate that, since the crystal-poor late-erupted Bishop Tuff contains less than 10% crystals, the impact of disregarding crystals is less than 5% in most cases and thus can be disregarded without significant impact.

Porosity Plots

Once porosity was calculated for each tomographic volume, I exploited the fact that, for each unit, there exist four porosity measurements of samples of increasing volume. Our expectation, based on the fact that each pumice piece can only contain vesicles smaller than its total size, was that we could derive vesicle size distributions from the measured porosity values. In other words, the smallest pumice piece only contains the smallest size bubbles in the population. The largest pumice piece would, in contrast, be large enough to contain the largest bubbles as well as the smallest and all the bubble in between (Figure 14). By plotting the size of the sample against its porosity for each pumice piece from the same sample, a cumulative porosity distribution is achieved.

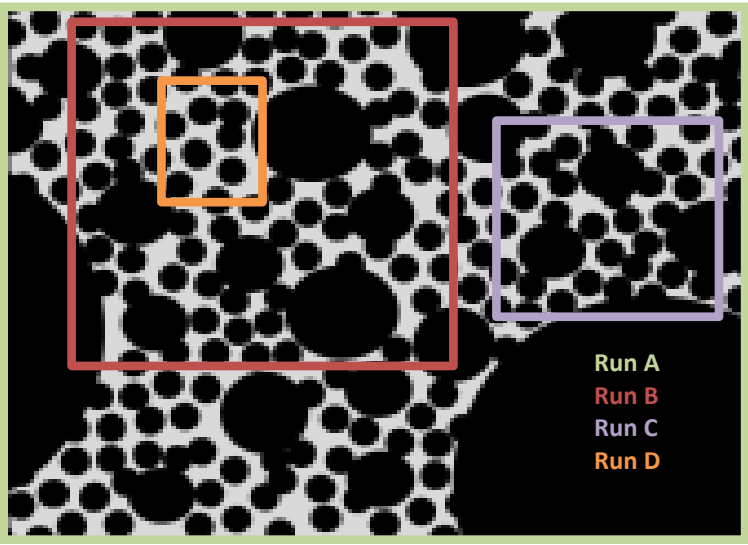

Figure 14. Cartoon showing the different bubble sizes able to be fitted into each sample size.

CHAPTER III

RESULTS

Volume And Bulk Density

Values arrived at using the convex hull method were generally larger than those of the perimeter difference or morph close by 2-3% due to forced inclusion of concavities in the sample without exception (Figure 15a). The perimeter difference method generally yielded the smallest values since this method takes into account only the width of the sample on each individual line of pixels, not how that width relates to rows around it, and so a majority of concavities and vesicles open to the sample margin were excluded from the volume in this calculation, removing all partial bubbles from the count (Figure 15b). Despite these differences, calculated bulk density and porosity were within 5% of one another (Table 4).

Figure 15. Illustrations showing the limitations of different volume determination methods . a) The convex hull cannot accommodate concavities within sample, adding excess volume. B) irregularities in the margins can cause omissions of volume with the perimeter difference method.

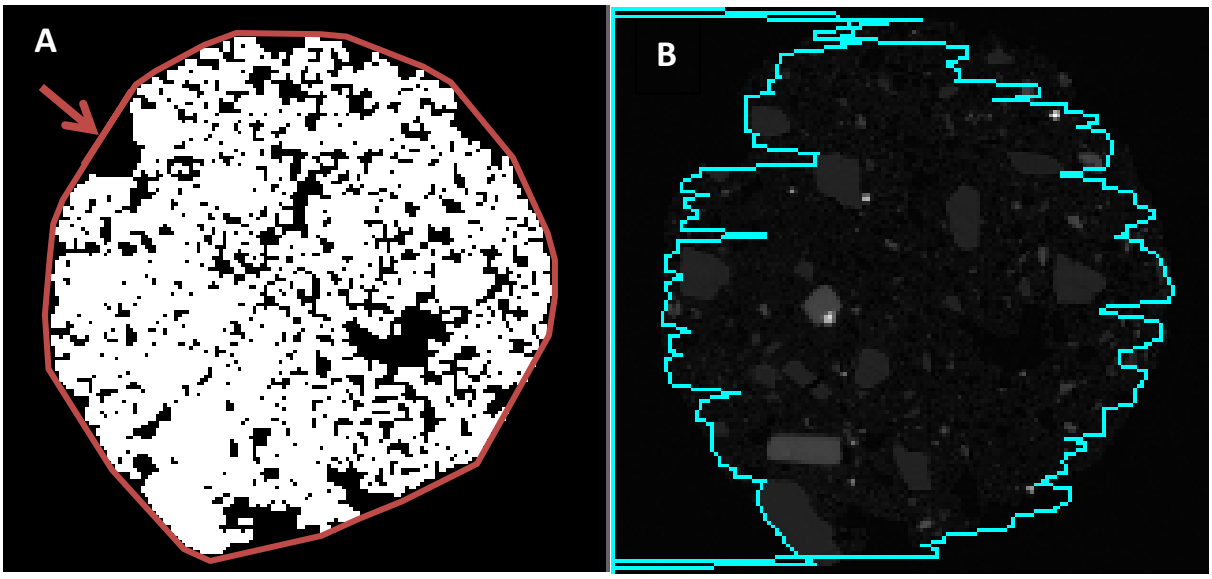

sample/run	% Porosity Convex Hull	morph	perimeter	Max porosity	Min Porosity	Difference
lg_955						
Run A	79.80	78.82	78.81	79.80	78.81	0.99
Run B	79.97	79.83	79.77	79.97	79.77	0.20
Run C	78.44	76.99	80.17	80.17	76.99	3.19
Run D	73.95	70.60	70.68	73.95	70.60	3.35
AB_6202						
Run A	72.74	70.08	71.06	72.74	70.08	2.66
Run B	75.34	73.52	75.21	75.34	73.52	1.83
Run C	77.50	77.10	77.66	77.66	77.10	0.57
Run D	73.28	71.00	72.18	73.28	71.00	2.28
Run F	71.94	68.97	69.06	71.94	68.97	2.97
F7_11						
Run A	71.06	69.71	71.97	71.97	69.71	2.26
Run B	72.88	70.07	71.71	72.88	70.07	2.81
Run C	72.15	71.37	71.83	72.15	71.37	0.78
Run F	66.63	61.85	62.91	66.63	61.85	4.79
AB_5301						
Run A	63.06	57.17	57.08	63.06	57.08	5.98
Run B	63.97	62.13	61.76	63.97	61.76	2.21
Run C	57.04	53.06	54.65	57.04	53.06	3.98
Run E	52.60	49.87	50.10	52.60	49.87	2.73
Run F	55.84	52.91	54.04	55.84	52.91	2.93
AB_xx02						
Run A	75.77	70.45	74.56	75.77	70.45	5.33
Run F	74.61	72.03	72.45	74.61	72.03	2.58
Run B	74.73	73.85	75.29	75.29	73.85	1.43
Run C	73.01	71.85	72.79	73.01	71.85	1.16
Run D	69.54	71.96	70.18	71.96	69.54	2.42

Table 4. Porosity Calculations as determined using three different methods. The max and minimum for each run is subtracted to find the total difference between the three.

Cumulative Porosity Plots

The smallest pumice chip for each sample has the smallest porosity when compared to the larger chips from that sample. For all samples the size of the smallest chip is the size of the "Run D" chip in figure 10. Run D-sized pumice chips, though they contain only the smallest bubbles of the population, are already >50% pore space. We expected, based on the rules of a cumulative distribution, that the porosity would continuously increase with increasing chip size; however, in reality, we observe a maximum porosity at and intermediate pumice chip size (Figure 16). The amount of decrease with increasing chip size varies, as does the sample size at which it begins. By nature and definition a cumulative plot cannot decrease with increasing sample size, as the new is always added to the previous with no subtraction, therefore these plots are either not, in fact cumulative porosity plots, or the data are being influenced by some outside process of collection or processing.

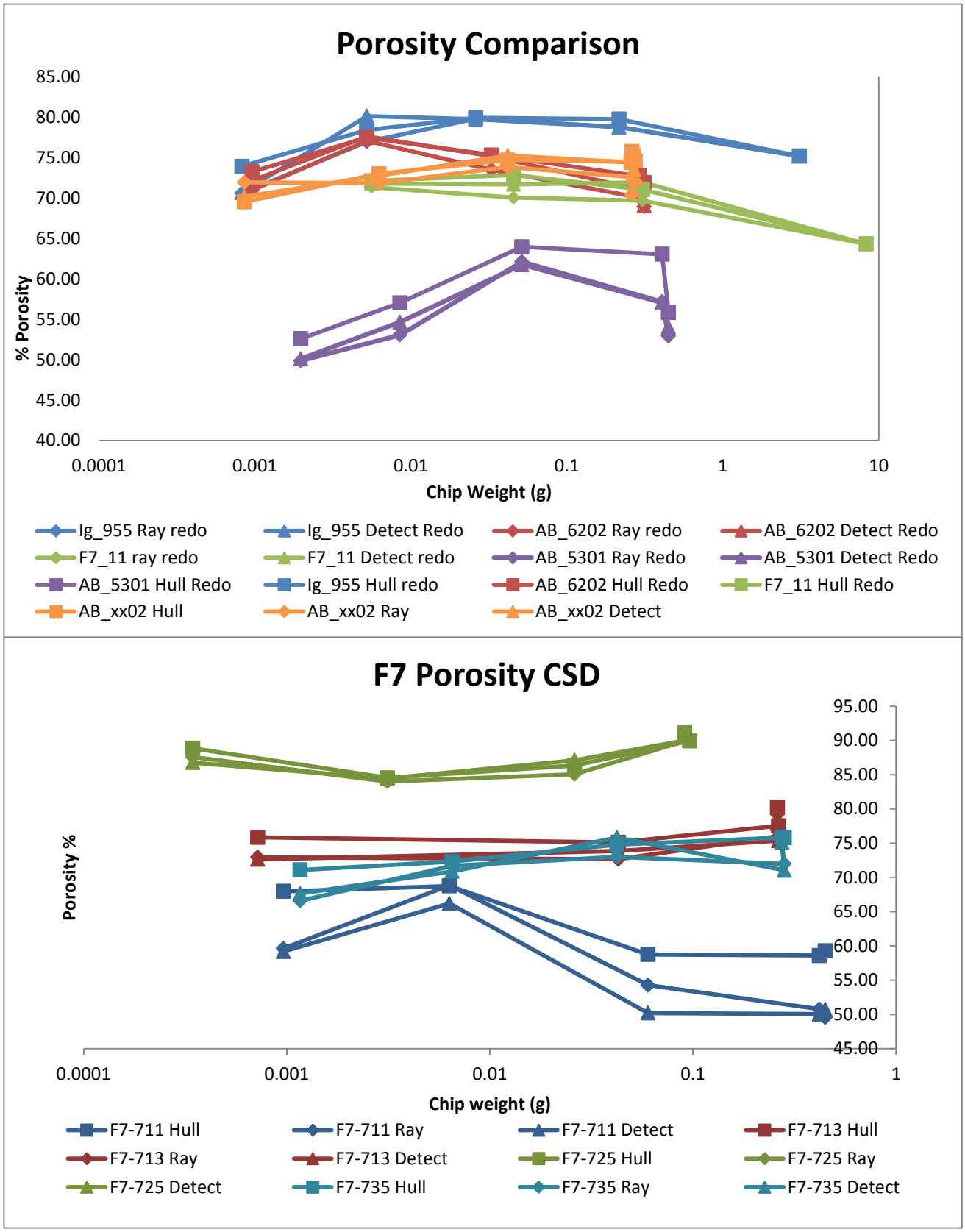

Figure 16. Cumulative porosity plots from tomogram analysis. Top, samples from various units. Bottom, all samples from unit F7. Same colored lines identify one sample. Same marker shape identifies one processing method.

CHAPTER IV

DISCUSSION

Syn-Eruptive Bubble Growth In The Bishop Tuff Magma

The fact that all three methods of volume calculation agree within 1-5% gives support to the notion that 3D tomograms can be reliably used in volume calculations. Calculations adding crystal density reveal that the abundance of crystals typically seen in the Bishop Tuff pumice has little to no effect on porosity estimations (Table 3). This means that in this study, crystals can be safely disregarded.

It is evident through images and preliminary porosity data that the vesicles in the Bishop Tuff pumice clasts vary significantly in size. Porosity calculations reveal that the smallest bubble size fraction (<10 μm) makes up over 50 vol.% of the total bubble population as evidenced by the fact that the smallest pumice chip, Run D, contains over 50% pore space. The size of these bubbles, >~10 μm, is not indicative of long growth histories meaning it is unlikely they formed long before eruption.

Truncated Distributions And Censored Data

The presence of a maximum in the cumulative porosity plot against size identified in the results section represents a situation that is physically impossible. When increasingly large bubbles are added to the bubble population, the total population should continually increase and asymptotically approach the maximum percentage of volume available. The trend that

appears in the porosity data acquired here suggests that adding pore space to the sample is resulting in a net loss of porosity as a whole. Because it is clear that this situation cannot physically take place, an explanation must be found by exploring the theoretical ideas behind the original hypothesis and the statistical relationships involved in creating the distribution of bubble sizes that results.

When investigating the statistical nature of the bubble distribution present in Bishop Tuff pumice, it is helpful to speak in terms of number of individual bubbles rather than combined porosity. As established above, small bubbles make up greater than 50% of the total cumulative porosity. This means there is a very large number of bubbles of this size and a very large nucleation density necessary to achieve that amount of porosity regardless of the total sample size. When larger bubbles are introduced, by default that means that less space is available in that sample to hold small bubbles. Unless the volume of the sample increases enough to hold both large bubbles and maintain the number density of small bubbles in the sample, the total effect of adding large bubbles to the population will be overpowered by the loss of small bubbles. Again this seems physically impossible, because a large bubble means more pore space in less volume than if that same porosity was reached with only small bubbles since no volume is lost to bubble walls made of glass. However, the problem with this logic lies in the fact that large bubbles are rare relative to small bubbles and the largest samples used in this study, 1 cm, are still smaller than the largest bubbles found in our samples. Because we desire samples of equant shape and dimension, and because it is more likely that tomographic processing will accurately calculate the volume and porosity of samples where a majority of the bubbles are enclosed within the sample by glass, large bubbles have been inadvertently

excluded from the samples in this study. Areas of the sample where large bubbles are prevalent were not sampled because the pieces would have contained large concavities and much of the volume would be pore space not enclosed by glass and difficult to quantify. Because the larger bubbles have dimensions as large as ¼ the total sample width, most are truncated by the sample boundaries (Figure 17). As the size of bubbles increases, these effects

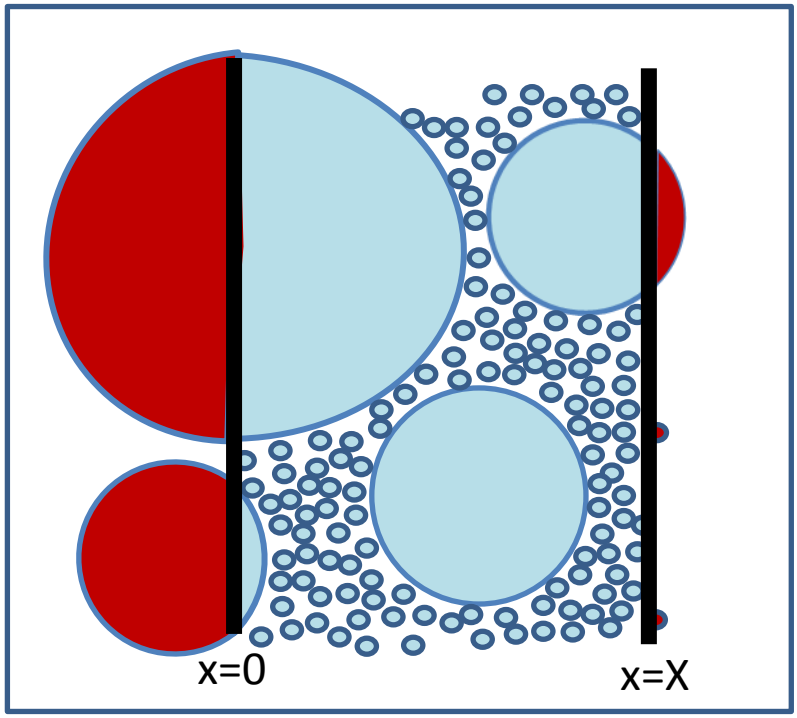

Figure 17. Cartoon showing the detrimental effect of samples much smaller than the largest bubbles in attempting to capture the influence of increasing bubble size on overall porosity. Blue represents captured porosity, red is lost porosity.

become more and more pronounced. The preferential exclusion of part or whole bubbles of sufficient size is known as censorship of the data (Furbish 1997 and unpublished). Though the increasing porosity exists in the unit as a whole, the size of our samples does not increase rapidly enough to accommodate it. When the sample size reaches a size where the proportion of large bubbles included effectively equals the proportion of large bubbles excluded, then the

cumulative porosity will once again reflect physical reality and porosity will again increase on the plot. In the case of this study, our samples do not reach that plateau, but a mathematical relationship was derived by David Furbish that describes this censoring effect on an underlying exponential distribution and thus can extrapolate the trend out to the samples sizes one would need in order to reach that point. The equation is as follows:

$$\boldsymbol{\varphi(X)} = N_x * {\mu_{vb}}^*$$

where $\varphi(X)$ is porosity of the sample, N_x is the number density of bubbles of a certain size and ${\mu_{vb}}^*$ is the average censored volume of a bubble. To solve this equation, ${\mu_{vb}}^*$ must first be calculated using:

$$\boldsymbol{{\mu_{vb}}^*} = -\frac{a{\mu_R}^3}{G}\left[e^{\frac{-X}{2\mu_R}}\left(\frac{X^3}{8{\mu_R}^3}+\frac{3X^2}{4{\mu_R}^2}+\frac{3X}{\mu_R}+6\right)-6\right] + \frac{2a{\mu_R}^4}{GX}\left[e^{\frac{-X}{2\mu_R}}\left(\frac{X^4}{16{\mu_R}^4}+\frac{X^3}{2{\mu_R}^3}+\frac{3X^2}{{\mu_R}^2}+\frac{12X}{\mu_R}+24\right)-24\right]$$

where *a* and *G* are constants, and μ_R is the average bubble radius. By solving this equation for all sample sizes we can infer what the ideal censored distribution would look like (Figure 18). This plot correlates with our observed porosity data within 2 standard deviations, and also contains a dip in cumulative porosity like that observed, suggesting that this idea of censoring may accurately describe the departure in our data. Currently, the mathematical explanation developed is intended to be used in fitting a dataset of multiple samples, and thus is likely not appropriate for fitting individual samples. To continue our work we must revisit the mathematical calculations and find a way to use the underlying cumulative distribution we have

fitted to either correct our individual censored samples or help us understand the bubble distributions in spite of the censoring effect.

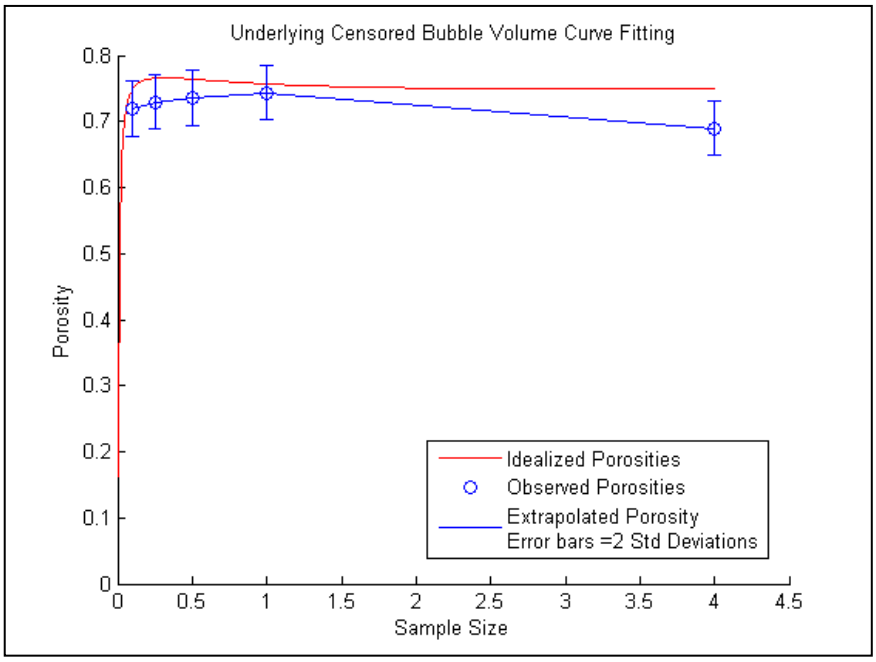

Figure 18. Plot of sample size versus porosity showing a comparison of observed distribution and statistically derived censored distribution. Blue line represents the average porosity observed for each size sample with error bars. Red line represents the derived distribution hypothesized to describe the observed distribution. The model appears to approximate the observed data within error.

CHAPTER V

CONCLUSIONS

The prevalence of wide size variation between largest and smallest bubbles present in Bishop Tuff pumice suggests that the small size fraction of the population grew very quickly relative to other bubbles and thus may very likely represent the results of decompression exsolution during eruption of the magma. Preliminary results using tomogram processing to obtain volume and porosity prove theoretically sound though more complicated than originally expected. Due to the size chosen for our samples, a statistical relationship results in a pseudo-decrease in porosity with increasing volume that can be explained by data censorship related to the relationship between sample size and maximum bubble radius. Though an ideal censored distribution can be calculated that represents our data, the usefulness of this information and the next steps toward obtaining a correct cumulative bubble size distribution are still unclear. The next steps are to revisit the mathematical explanation of the censored distribution and find a way to use it appropriately for fitting individual samples rather than a population.

GENERAL CONCLUSIONS

Pumice clasts from the Bishop Tuff contain several lines of evidence that can be used to interpret the syn-eruptive processes associated with the eruption as a whole and the individual depositional units. Through textural and petrographic analysis and experimental decompressions it can be shown that the Bishop Tuff magma body was decompressed at two distinct rates, likely over the course of six days or more. A slower rate of decompression fostered the growth of microlite quartz crystals 1-50 μm in size, compositionally distinct quartz rims on pre-existing phenocrysts, and irregular quartz growth interstitially among feldspars. The faster decompression phase is needed for bubble nucleation to thrive and vesicles less than 10 μm to dominate the volume. With the analysis of more experimental products, better constraints on time and temperature will be established. In addition, experiments beginning with crystal-fee ash material are planned to better approximate the composition of melt available for microlite growth, which may bolster those conclusions we have drawn thus far.

Though the method of vesicle size distribution determination originally conceived yields neither an expected nor accurate result, the theory and statistical work thus far performed suggests that valuable information may still be gleaned from censored cumulative bubble size distributions. By understanding the impact of censorship taking place, it may be possible to correct for the effect by back-calculating an uncensored distribution or by normalizing the effect, making its influence standard across all samples. The differences in the mathematical description of individual samples versus the total population must be understood for this task to progress.

REFERENCES

Armienti, P, Pareschi, MT, Innocenti, F, Pompilio, M, Effects of magma storage and ascent on the kinetics of crystal growth, Contributions to Mineral Petrology, 115, p. 402-414, 1994.

Anderson, AT, Davis, AM, Lu, F, Evolution of the bishop tuff rhyolitic magma based on melt and magnetite inclusions and zoned phenocrysts, Journal of Petrology, 41, p. 449-473, 2000.

Bailey, RA, Dalrymple, GB, Lanphere, MA, Volcanism, Structure, and geochronology of Long Valley caldera, Mono county, California, Journal of Geophysical Research, 81, p. 725-744, 1976.

Baker, DR, Mancini, M, Polacci, M, Higgins, MD, Gualda, GAR, Hill, RJ, Rivers, ML, An introduction to the application of x-ray microtomography to the three-dimensional study of igneous rocks, Lithos, 148, p. 262-276, 2012.

Blundy, J, Cashman, KV, Ascent-driven crystallization of dacite magmas at mount st. Helens, 1980-1986, Contributions to Mineral Petrology, 140, p. 631-650, 2001.

Cashman, KV, Groundmass crystallization of mount st. helens dacite 1980-1986—a tool for interpreting shallow magmatic processes, Contributions to Mineral Petrology, 109,431-449, 1992.

Crowley, JL, Schone, B, Bowring, SA, U-Pb dating of zircon in the bishop tuff at the millennial scale, Geology, 35, p. 1123-1126, 2007.

Dunbar, NW, Hervig, RL, Petrogenesis and volatile stratigraphy of the bishop tuff: evidence from melt inclusion analysis, Journal of Geophysical Research, 97, 1992.

Francis, P, Oppenheimer, C, Volcanoes: second edition, Oxford University Press, New York, print, 2004.

Furbish, DJ, Fluid Physics in Geology, Oxford University Press, New York, print, 1997.

Gardner, JE, Sigurdsson, H, Carey, SN, Eruption dynamics and magma withdrawal during the plinian phase of the Bishop Tuff eruption, Long Valley caldera, Journal of Geophysical Research, 26, p. 8097-8111, 1991.

Gardner, JE, Hilton, M, Carroll, MR, Experimental constraints on degassing of magma:

isothermal bubble growth during continuous decompression from high pressure, Earth and Planetary Science Letters, 168, p. 201-218, 1999.

Gilbert, CM, Welded tuff in eastern California, Bulletin of the Geological Society of America, 49, p. 1829-1862, 1938.

Gualda, GAR, Cook, DL, Chopra, R, Qin, LP, Anderson, AT Jr., Rivers, M, Fragmentation, nucleation, and migration of crystals and bubbles in the Bishop Tuff rhyolitic magma, Transactions of the Royal Society of Edinburgh, Earth Sciences, 95, p. 375-390, 2004.

Guslda, GAR, Rivers, M, Quantitative 3D petrography using x-ray tomography: application to bishop tuff pumice clasts, 154, p. 48-62, 2006,

Gualda, GAR, Anderson, AT Jr., Magnetite Scavenging and the buoyancy of bubbles in magmas. Part 1: discovery of a pre-eruptive bubble in Bishop rhyolite, Contributions to Mineral Petrology, 153, p. 733-742, 2007.

Gualda, GAR, Crystal and bubble populations in the early erupted Bishop rhyolitic magma: microscopy, X-ray tomography, and microanalysis of pumice clasts, PhD Thesis, University of Chicago, 2007.

Gualda, GAR, Anderson, AT Jr., Sutton, SR, Rapid Crystallization of the Bishop magma, EOS Transactions, American Geophysical Union, 87, Fall Meeting Supplement, Abstract V24C-04, 2007.

Gualda, GAR, Baker, DB, Polacci, M, Introduction : advances in 3D imaging and analysis of geomaterials, Geosphere, 6, p. 468-469, 2010.

Gualda GAR, Pamukcu, AS, Ghiorso MS, Anderson AT Jr, Sutton SR, Timescales of Quartz Crystallization and the Longevity of the Bishop Giant Magma Body, PLoSONE, 2012.

Gualda, GAR, Ghiorso, MS, The bishop tuff giant magma body: an alternative to the standard model, Contributions to Mineral Petrology, 166, p. 755-775, 2013.

Hildreth, W, The magma chamber of the Bishop Tuff: gradients in temperature, pressure, and composition, PhD Thesis, University of California Berkeley, 1979.

Hildreth, W, Wilson, CJ, Compositional zoning of the bishop tuff, Journal of Petrology, 48, 951-999, 2007.

Larsen, JF, Denis, M, Gardner, JE, Experimental study of bubble coalescence in rhyolitic and phonolitic melts, Geochimica et Cosmochimica Acta, 68, p. 333-344, 2004.

Mangan, MT, Cashman, KV, Newman, S, Vesiculation of basaltic magma during eruption, Geology, 21, p. 157-160, 1993.

Matthews, NE, Pyle, DM, Smith, VC, Wilson, CJN, Huber, C, van Hinsberg, V, Quartz zoning and the pre-eruptive evolution of the 340-ka Whakamaru magma systems, new Zealand, Contributions to Mineralogy and Petrology, 163, 87-107, 2012a.

Miller, CF, Wark, DA, Supervolcanoes and their explosive Supereruptions, Elements, 4, 1, p. 11-15, 2008

Pamukcu, AS, Gualda, GAR, Anderson, AT Jr., Crystallization stages of the Bishop Tuff magma body recorded in crystal texture in pumice clasts, Journal of Petrology, 53, 3, p. 589-609, 2012.

Pamukcu, AS, Gualda, GAR, Quantitative 3D petrography using X-ray tomography 2: combining information at various resolutions, Geosphere, 6,6, p. 775-781, 2010.

Simon, JI, Reid, MR, The pace of rhyolite differentiation and storage in an 'archetypical' silicic magma system, Long Valley, Californian, Earth and Planetary Science Letters, 235, p. 123-140, 2005.

Sparks, RSJ, The dynamics of bubble formation and growth in magmas: a review and analysis, Journal of Volcanology Geothermal Research, 3, p. 1-37, 1978.

Sparks, RSJ, Brazier, S, New evidence for degassing processes during explosive eruptions, Nature, 295, p. 21-23, 1982.

Voltolini, M, Zandomeneghi, D, Mancini, L, Polacci, M, tecture analysis of volcanic rock samples: quantitative study of crystals and vesicles shape preferred orientation from x-ray microtomography data, 202, p. 83-95, 2011.

Wallace, PJ, Anderson, AT Jr., Davis, AM, Quantification of pre-eruptive exsolved gas contents in silicic magmas, Nature, 377, p. 612-616, 1995.

Wallace, PJ, Anderson, AT, Davis AM, Gradients in H_2O, CO_2 and exsolved gas in a large-volume silicic magma system: interpreting the record preserved in melt inclusions from the bishop tuff, Journal of Geophysical Research, 104, p. 20,097-20,122. 1999.

Wark, DA, Hildreth, W, Spear, FS, Cherniak, DJ, Watson, EB, Pre-eruption recharge of the bishop magma system, Geology, 35, 3, p. 235-238, 2007.

Wilson, CJN, Hildreth, W, The Bishop Tuff: new insights from eruptive stratigraphy, Journal of Geology, 105, p. 407-439, 1997.

Wilson, CJN, The 26.5 ka Oruanui eruption, New Zealand: an introduction and overview, Journal of Volcanology and Geothermal Research, 112, p. 133–174, 2001.

Wilson, L Sparks, RSJ, Walker, GPL, Explosive volcanic eruptions, IV, the control of magma properties and conduit geometry on eruption column behavior, Geophysical Journal of the Royal Astronomical Society, 63, p. 117-148, 1980.

Wilson, L, Head, JW, Ascent and eruption of basaltic magma on the earth and moon, Journal of Geophysical Research, 86, p. 2971-3001, 1981.

APPENDIX A

Volume, Bulk Density, and Porosity data for Bishop Tuff Pumice clasts

Table A1, Volume measures in pixels for each volume method

	Volume					
sample/run	**Convex Hull**		**Ray Detect**		**Sample Detect**	
	full	0.25	Full	0.25	full	0.25
Ig_955 REDO						
Clast						
Run A	9.48E+07	1.48E+06	9.04E+07	1.41E+06	9.03E+07	1.41E+06
Run B	8.89E+07	1.39E+06	8.83E+07	1.38E+06	8.80E+07	1.38E+06
Run C	1.24E+08	1.94E+06	1.17E+08	1.82E+06	1.35E+08	2.11E+06
Run D	8.83E+07	1.38E+06	7.83E+07	1.22E+06	7.85E+07	1.23E+06
AB_6202 REDO	0.00E+00					
Run A	9.50E+07	1.48E+06	8.65E+07	1.35E+06	8.95E+07	1.40E+06
Run B	9.12E+07	1.42E+06	8.49E+07	1.33E+06	9.07E+07	1.42E+06
Run C	1.19E+08	1.86E+06	1.17E+08	1.83E+06	1.20E+08	1.88E+06
Run D	1.00E+08	1.56E+06	9.22E+07	1.44E+06	9.61E+07	1.50E+06
Run F	9.88E+07	1.54E+06	8.94E+07	1.40E+06	8.96E+07	1.40E+06
	0.00E+00					
F7_11 REDO	0.00E+00					
Clast						
Run A	9.37E+07	1.46E+06	8.95E+07	1.40E+06	9.68E+07	1.51E+06
Run B	1.15E+08	1.80E+06	1.04E+08	1.63E+06	1.10E+08	1.72E+06
Run C	1.04E+08	1.62E+06	1.01E+08	1.57E+06	1.02E+08	1.60E+06
Run F	9.55E+07	1.49E+06	8.36E+07	1.31E+06	8.60E+07	1.34E+06
AB_5301 REDO						
Run A	9.77E+07	1.53E+06	8.43E+07	1.32E+06	8.41E+07	1.31E+06
Run B	9.78E+07	1.53E+06	9.30E+07	1.45E+06	9.22E+07	1.44E+06
Run C	1.02E+08	1.59E+06	9.32E+07	1.46E+06	9.65E+07	1.51E+06
Run E	1.09E+08	1.70E+06	1.03E+08	1.61E+06	1.04E+08	1.62E+06
Run F	8.84E+07	1.38E+06	8.29E+07	1.30E+06	8.50E+07	1.33E+06
AB_XX02	0.00E+00		0.00E+00		0.00E+00	
Run A	9.56E+07	1.49E+06	7.83E+07	1.22E+06	9.10E+07	1.42E+06
Run F	9.41E+07	1.47E+06	8.54E+07	1.33E+06	8.67E+07	1.36E+06
Run B	1.13E+08	1.76E+06	1.09E+08	1.71E+06	1.15E+08	1.80E+06
Run C	1.19E+08	1.86E+06	1.14E+08	1.78E+06	1.18E+08	1.85E+06
RunD	7.83E+07	1.22E+06	8.51E+07	1.33E+06	8.00E+07	1.25E+06
Run K	9.63E+07	1.50E+06	8.57E+07	1.34E+06	9.03E+07	1.41E+06
Run P	8.98E+07	1.40E+06	8.36E+07	1.31E+06	8.94E+07	1.40E+06
F7-711						
Run A	9.74E+07	1.52E+06	7.87E+07	1.23E+06	8.05E+07	1.26E+06
Run F	8.82E+07	1.38E+06	7.41E+07	1.16E+06	7.30E+07	1.14E+06
Run B	9.97E+07	1.56E+06	8.99E+07	1.40E+06	8.26E+07	1.29E+06
Run C	1.04E+08	1.63E+06	1.04E+08	1.63E+06	9.61E+07	1.50E+06

Table A1, Cont.

Run D	8.36E+07	1.31E+06	6.63E+07	1.04E+06	6.56E+07	1.02E+06
F7-713						
Run A	1.17E+08	1.83E+06	1.11E+08	1.73E+06	1.04E+08	1.63E+06
Run F	1.02E+08	1.60E+06	9.57E+07	1.50E+06	9.32E+07	1.46E+06
Run B	1.18E+08	1.84E+06	1.07E+08	1.68E+06	1.12E+08	1.76E+06
Run D	8.31E+07	1.30E+06	7.41E+07	1.16E+06	7.33E+07	1.15E+06
F7-725						
Run A	9.06E+07	1.41E+06	8.46E+07	1.32E+06	8.89E+07	1.39E+06
Run F	8.33E+07	1.30E+06	8.50E+07	1.33E+06	8.49E+07	1.33E+06
Run B	1.31E+08	2.04E+06	1.20E+08	1.87E+06	1.38E+08	2.16E+06
Run C	1.04E+08	1.63E+06	1.00E+08	1.57E+06	1.03E+08	1.62E+06
Run D	8.61E+07	1.35E+06	7.72E+07	1.21E+06	7.25E+07	1.13E+06
F7-735						
Run A	1.01E+08	1.57E+06	9.80E+07	1.53E+06	9.77E+07	1.53E+06
Run F	1.01E+08	1.58E+06	8.74E+07	1.37E+06	8.45E+07	1.32E+06
Run B	1.14E+08	1.79E+06	1.07E+08	1.67E+06	1.19E+08	1.87E+06
Run C	1.21E+08	1.89E+06	1.19E+08	1.85E+06	1.15E+08	1.80E+06
Run D	1.12E+08	1.75E+06	9.70E+07	1.51E+06	1.00E+08	1.56E+06

Table A2, Conversion of pixel counts to cubic centimeters

	pixel to distance conversion			True volume (cm^3)					
								Sample	
sample/run	resolution		vol/pix	Convex Hull		Ray Detect		Detect	
	microns	cm	cm	Full	0.25	full	0.25	full	0.25
Ig_955 REDO									
Clast									
Run A	17	0.0017	4.913E-09	0.466	0.007	0.444	0.007	0.444	0.007
Run B	8.6	0.00086	6.3606E-10	0.057	0.001	0.056	0.001	0.056	0.001
Run C	4.39	0.00044	8.4605E-11	0.011	0.000	0.010	0.000	0.011	0.000
Run D	2.5	0.00025	1.5625E-11	0.001	0.000	0.001	0.000	0.001	0.000
AB_6202 REDO	0			0.000	0.000				
Run A	17	0.0017	4.913E-09	0.467	0.007	0.425	0.007	0.440	0.007
Run B	8.6	0.00086	6.3606E-10	0.058	0.001	0.054	0.001	0.058	0.001
Run C	4.39	0.00044	8.4605E-11	0.010	0.000	0.010	0.000	0.010	0.000
Run D	2.5	0.00025	1.5625E-11	0.002	0.000	0.001	0.000	0.002	0.000
Run F	17	0.0017	4.913E-09	0.486	0.008	0.439	0.007	0.440	0.007
F7_11 REDO									
Clast									
Run A	17	0.0017	4.913E-09	0.460	0.007	0.440	0.007	0.475	0.007
Run B	8.6	0.00086	6.3606E-10	0.073	0.001	0.066	0.001	0.070	0.001
Run C	4.39	0.00044	8.4605E-11	0.009	0.000	0.009	0.000	0.009	0.000
Run F	17.1	0.00171	5.0002E-09	0.478	0.007	0.418	0.007	0.430	0.007
				0.000	0.000				
AB_5301 REDO					0.000				
Run A	17	0.0017	4.913E-09	0.480	0.008	0.414	0.006	0.413	0.006
Run B	8.6	0.00086	6.3606E-10	0.062	0.001	0.059	0.001	0.059	0.001
Run C	4.39	0.00044	8.4605E-11	0.009	0.000	0.008	0.000	0.008	0.000
Run E	2.55	0.00026	1.6581E-11	0.002	0.000	0.002	0.000	0.002	0.000
Run F	17.1	0.00171	5.0002E-09	0.442	0.007	0.415	0.006	0.425	0.007
AB_XX02		0	0	0.000	0.000	0.000	0.000	0.000	0.000
Run A	17	0.0017	4.913E-09	0.470	0.007	0.385	0.006	0.447	0.007
Run F	17.1	0.00171	5.0002E-09	0.470	0.007	0.427	0.007	0.434	0.007
Run B	8.6	0.00086	6.3606E-10	0.072	0.001	0.069	0.001	0.073	0.001
Run C	4.39	0.00044	8.4605E-11	0.010	0.000	0.010	0.000	0.010	0.000
RunD	2.5	0.00025	1.5625E-11	0.001	0.000	0.001	0.000	0.001	0.000
Run K	17	0.0017	4.913E-09	0.473	0.007	0.421	0.007	0.444	0.007
Run P	17	0.0017	4.913E-09	0.441	0.007	0.411	0.006	0.439	0.007
F7-711									

Table A2, Cont.

Run A	17	0.0017	4.913E-09	0.478	0.007	0.386	0.006	0.395	0.006
Run F	17.1	0.00171	5.0002E-09	0.441	0.007	0.371	0.006	0.365	0.006
Run B	8.6	0.00086	6.3606E-10	0.063	0.001	0.057	0.001	0.053	0.001
Run C	4.39	0.00044	8.4605E-11	0.009	0.000	0.009	0.000	0.008	0.000
Run D	2.5	0.00025	1.5625E-11	0.001	0.000	0.001	0.000	0.001	0.000
F7-713									
Run A	17	0.0017	4.913E-09	0.574	0.009	0.545	0.009	0.512	0.008
Run F	17.1	0.00171	5.0002E-09	0.511	0.008	0.479	0.007	0.466	0.007
Run B	8.6	0.00086	6.3606E-10	0.075	0.001	0.068	0.001	0.072	0.001
Run D	2.5	0.00025	1.5625E-11	0.001	0.000	0.001	0.000	0.001	0.000
F7-725									
Run A	17	0.0017	4.913E-09	0.445	0.007	0.416	0.006	0.437	0.007
Run F	17.1	0.00171	5.0002E-09	0.417	0.007	0.425	0.007	0.425	0.007
Run B	8.6	0.00086	6.3606E-10	0.083	0.001	0.076	0.001	0.088	0.001
Run C	4.39	0.00044	8.4605E-11	0.009	0.000	0.008	0.000	0.009	0.000
Run D	2.5	0.00025	1.5625E-11	0.001	0.000	0.001	0.000	0.001	0.000
F7-735									
Run A	17	0.0017	4.913E-09	0.494	0.008	0.482	0.008	0.480	0.007
Run F	17.1	0.00171	5.0002E-09	0.506	0.008	0.437	0.007	0.422	0.007
Run B	8.6	0.00086	6.3606E-10	0.073	0.001	0.068	0.001	0.076	0.001
Run C	4.39	0.00044	8.4605E-11	0.010	0.000	0.010	0.000	0.010	0.000
Run D	2.5	0.00025	1.5625E-11	0.002	0.000	0.002	0.000	0.002	0.000

Table A3, Bulk Density and porosity calculations for Bishop Tuff pumice clasts

		Bulk Density			% Porosity		
sample/run	Weight	Hull	Ray	Detect	Hull	Ray	Detect
lg_955 REDO							
Clast					75.22	75.22	75.22
Run A	0.216	0.46	0.49	0.49	79.80	78.82	78.81
Run B	0.026	0.46	0.46	0.47	79.97	79.83	79.77
Run C	0.005	0.50	0.53	0.46	78.44	76.99	80.17
Run D	0.001	0.60	0.68	0.67	73.95	70.60	70.68
AB_6202 REDO	0.000						
Run A	0.293	0.63	0.69	0.67	72.74	70.08	71.06
Run B	0.033	0.57	0.61	0.57	75.34	73.52	75.21
Run C	0.005	0.52	0.53	0.51	77.50	77.10	77.66
Run D	0.001	0.61	0.67	0.64	73.28	71.00	72.18
Run F	0.313	0.65	0.71	0.71	71.94	68.97	69.06
F7_11 REDO							
Clast							
Run A	0.306	0.67	0.70	0.64	71.06	69.71	71.97
Run B	0.046	0.62	0.69	0.65	72.88	70.07	71.71
Run C	0.006	0.64	0.66	0.65	72.15	71.37	71.83
Run F	0.367	0.77	0.88	0.85	66.63	61.85	62.91
AB_5301 REDO							
Run A	0.408	0.85	0.99	0.99	63.06	57.17	57.08
Run B	0.052	0.83	0.87	0.88	63.97	62.13	61.76
Run C	0.009	0.99	1.08	1.04	57.04	53.06	54.65
Run E	0.002	1.09	1.15	1.15	52.60	49.87	50.10
Run F	0.449	1.02	1.08	1.06	55.84	52.91	54.04
AB_XX02							
Run A	0.262	0.56	0.68	0.59	75.77	70.45	74.56
Run F	0.275	0.58	0.64	0.63	74.61	72.03	72.45
Run B	0.042	0.58	0.60	0.57	74.73	73.85	75.29
Run C	0.006	0.62	0.65	0.63	73.01	71.85	72.79
RunD	0.001	0.70	0.64	0.69	69.54	71.96	70.18
Run K	0.269	0.57	0.64	0.61	75.22	72.16	73.60
Run P	0.259	0.59	0.63	0.59	74.52	72.62	74.41
F7-711							
Run A	0.448	0.94	1.16	1.13	59.26	49.57	50.71
Run F	0.420	0.95	1.13	1.15	58.60	50.76	50.04

Run B	0.060	0.95	1.05	1.15	58.76	54.26	50.20
Run C	0.006	0.72	0.72	0.78	68.75	68.85	66.19
Run D	0.001	0.74	0.93	0.94	67.97	59.63	59.18
F7-713							
Run A	0.261	0.45	0.48	0.51	80.25	79.21	77.85
Run F	0.264	0.52	0.55	0.57	77.53	76.01	75.36
Run B	0.043	0.57	0.63	0.60	75.11	72.65	73.87
Run D	0.001	0.56	0.62	0.63	75.85	72.94	72.63
F7-725							
Run A	0.091	0.20	0.22	0.21	91.09	90.46	90.93
Run F	0.096	0.23	0.23	0.23	89.93	90.13	90.12
Run B	0.026	0.31	0.34	0.30	86.35	85.06	87.10
Run C	0.003	0.36	0.37	0.36	84.55	83.98	84.45
Run D	0.000	0.26	0.29	0.30	88.85	87.56	86.76
F7-735							
Run A	0.274	0.55	0.57	0.57	75.87	75.24	75.16
Run F	0.281	0.56	0.64	0.67	75.82	71.99	71.03
Run B	0.042	0.58	0.62	0.56	74.78	73.00	75.83
Run C	0.007	0.64	0.65	0.67	72.30	71.71	70.88
Run D	0.001	0.66	0.77	0.74	71.10	66.59	67.65